TECHNISCHE UNIVERSITÄT WIEN

DIPLOMARBEIT

Mathematische Modellierung einer elektrostatischen Einölmaschine

zur Erlangung des akademischen Grades

Diplom-Ingenieur

im Rahmen des Studiums

Physikalische Energie- und Messtechnik

eingereicht von

Julian Landauer
Matrikelnummer 01402176

ausgeführt am Institut für Automatisierungs- und Regelungstechnik der Fakultät für Elektrotechnik und Informationstechnik der Technischen Universität Wien in Zusammenarbeit mit voestalpine

Betreuung
Betreuer: Univ.Prof. Dipl.-Ing. Dr.techn. Andreas Kugi
Co-Betreuer: Ao.Univ.Prof. Dipl.-Ing. Dr.techn. Martin Gröschl
Mitwirkung: Assistant Prof. Dipl.-Ing. Dr.techn. Andreas Steinböck

Wien, 16.12.2019

(Unterschrift Verfasser) (Unterschrift Betreuer)

Preamble

This diploma thesis titled Mathematical Modeling of an Electrostatic Oiling Machine was conducted at the Automation and Control Institute of TU Wien. I would like to express my gratitude to my supervisors Univ.-Prof. Dr. techn. Andreas Kugi, Assistant Prof. Dr. techn. Andreas Steinböck, and Univ.-Prof. Dr. techn. Martin Gröschl for their help with words and deeds. Further, I want to thank voestalpine for making this work possible. Finally, I want to give special thanks to my family, who were always supporting me during my entire studies and to everybody, who was encouraging and assisting me in this time.

Vienna, December 2019

Abstract

This diploma thesis deals with the mathematical modeling of the electrostatic spraying process in an industrial oiling machine. It is used to oil continuous steel strips on both sides. A typical electrostatic oiler consists of two oiling blades supplied with high voltage. Oil is pumped to these blades where it is atomized and sprayed on the strip surface due to the high electric field strength. A numerical model of the spraying process is developed in ANSYS Fluent which includes the electric field, the oil droplet trajectories and the air flow due to the movement of the droplets and the strip. In contrast to other works, a droplet breakup model is included which describes the breakup due to the charge carried by the droplets and due to the drag force. The model is validated using measurement data of an industrial oiling machine. Furthermore, the plausibility of the model is checked using the Rayleigh limit for the droplet size. The model captures the dependence of the oil droplet trajectories on the voltage, the amount of oil, the air flow, and the distance between the blade and the strip. The model can be used in simulations to give a valuable process insight for operators and researchers and to identify optimization possibilities. The negative effect of an inclined oiler blade on the oil distribution on the strip is discussed in more detail and some improvements are proposed.

Kurzzusammenfassung

Die vorliegende Diplomarbeit beschäftigt sich mit der mathematischen Modellierung des elektrostatischen Sprühprozesses in einer industriellen Einölmaschine. Derartige Einölmaschinen werden zum Auftragen eines Ölfilms auf Stahlbänder verwendet. Eine elektrostatische Einölmaschine besteht aus zwei Ölbalken, die mit Hochspannung versorgt werden. Öl wird zu den Ölbalken gepumpt und dort aufgrund der hohen elektrischen Feldstärke zerstäubt und auf das Band gesprüht. Im Zuge dieser Arbeit wird ein numerisches Modell in ANSYS Fluent erstellt, welches das elektrische Feld, die Trajektorien der Öltropfen und die Luftströmung zufolge der Tropfen- und der Bandbewegung berechnet. Im Gegensatz zu anderen Arbeiten wird der Zerfall der Tropfen während des Sprühprozesses mithilfe eines Breakup-Modells berücksichtigt. Zum Zerfall der Tropfen kommt es aufgrund der abstoßenden Kräfte zwischen den elektrischen Ladungen die sich auf der Tropfenoberfläche befinden und aufgrund der Luftreibung, die auf die Tropfen wirkt. Das Modell wird mithilfe von Messdaten von einer echten Anlage validiert. Des weiteren wird die Plausibilität der Simulationsergebnisse mithilfe des Rayleigh-Limits, welches die maximale Tropfengröße vorhersagt, überprüft. Das Modell erfasst die Abhängigkeit der Öltropfentrajektorien von der Spannung, von der Ölmenge, von der Luftströmung und vom Abstand zwischen Ölbalken und Stahlband. Das Modell kann verwendet werden um ein besseres Verständnis für den Einölprozess zu erhalten und um Optimierungsmöglichkeiten zu identifizieren. Des weiteren wird in dieser Arbeit der negative Einfluss der Schiefstellung des Ölbalkens auf die Ölverteilung am Band betrachtet und Verbesserungsvorschläge hierzu erarbeitet.

Contents

List of Figures

List of Tables

1 Introduction

Electrostatic spraying is used in many industrial applications such as powder coating, painting, or oiling. Electrostatic spraying systems are more efficient compared to systems that use brushes, rollers or airsprays. This thesis deals with an electrostatic oiling machine which is part of a hot dip galvanizing line where steel strips are galvanized. At the end of the galvanizing line an oil film is sprayed on the strips to passivate the surface. Furthermore, the oil film is used as a lubricant for subsequent forming processes. Due to their high complexity the optimization of electrostatic spraying processes is difficult. There are many powerful software tools to create models of such processes. Every model has to find a balance between computational complexity and the level of detail. An appropriate model can be used to improve the understanding of the process and to identify possibilities for optimization.

1.1 State of the Art

There are many articles published on the mathematical modeling of the electrostatic spraying process. Some essential equations to describe the electrostatic spraying of dielectric liquids are summarized in [1]. In this work, an electrostatic atomizer for diesel fuel is studied and experimentally improved. The development of a numerical model to simulate the trajectories of droplets generated by an electrostatic rotary bell atomizer is presented in [2]. FEMLAB is used to simulate the air flow and a custom C++ code to simulate the electric field and the droplet trajectories. A finite element method model of the electrostatic rotary Bell atomizer is presented in [3]. A numerical method developed for the calculation of the electric field and the particle trajectories for electrostatic powder coating is presented in [4] and [5]. ANSYS Fluent with user-defined functions is used to evaluate the electrostatic field under consideration of the space charge. In [6], a three-dimensional numerical ANSYS Fluent model of an electrostatic coating process that incorporates a moving mesh to simulate movements of the target is presented. The implementation of the electric field in ANSYS Fluent using user-defined functions is described in more detail in [7]. In [4], [5], and [6], a particle size distribution is used for the injected particles to get more accurate results. All the mentioned models do not consider a breakup of the particles. However, breakups occur especially in the case of droplets and they are important for the calculation of the exact trajectories.

1.2 Objectives of this Work

The aim of this thesis is to develop a numerical, two-dimensional, steady-state model of the electrostatic spraying process for a specific type of electrostatic oiling machine. The model should contribute to a better understanding of the electrostatic oiling process for operators and for future improvements. Moreover, possibilities to optimize the oiling process should be identified.

1.3 Structure of this Thesis

The main parts and the function of the considered electrostatic oiling machine are described in Chapter 2. The numerical model implemented in ANSYS Fluent and the underlying equations are presented in Chapter 3. Chapter 4 describes the measurements that were carried out for the validation of the model. This validation and some simulation results are summarized in Chapter 5. Chapter 6 deals with the effect of an inclined oiler blade on the oil distribution where the model is used to optimize the orientation of the blade. Chapter 7 contains some conclusions and suggestions for improvements and an outlook on future research activities in this field.

2 Structure and Function of the Electrostatic Oiler

This chapter describes the main parts of the considered electrostatic oiler and summarizes their function. Figures 2.1 and 2.2 show a two blade electrostatic oiler for the coating of continuous strips [8].

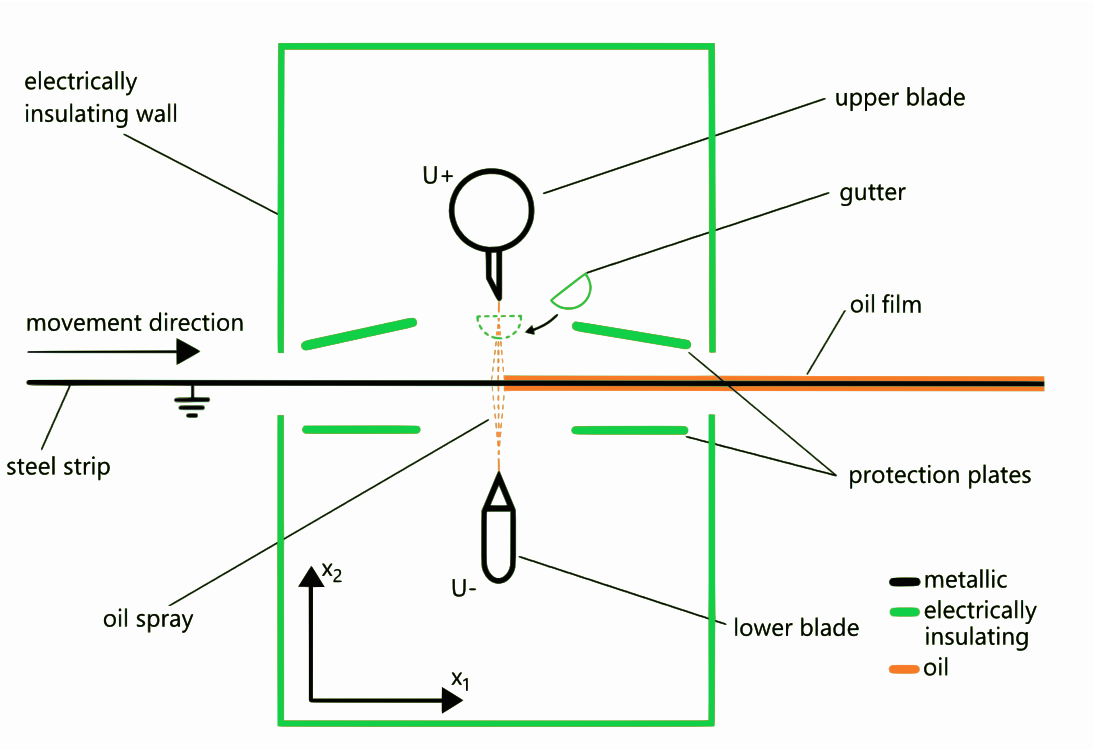

Figure 2.1: Cross section of the electrostatic oiler.

Basically, the electrostatic oiler consists of two oiling blades supplied with high voltage and an electrically insulating enclosure. The high voltage and the blade geometry lead to a high electric field strength at the blade tip. The steel strip is continuously conveyed through the enclosure and in this way is oiled on both sides. The protection plates protect the blades against strip impacts. This may happen e.g. when the previous trimming of the steel strip is faulty.

The oil which is sprayed on the steel strip has a high viscosity at ambient temperature.

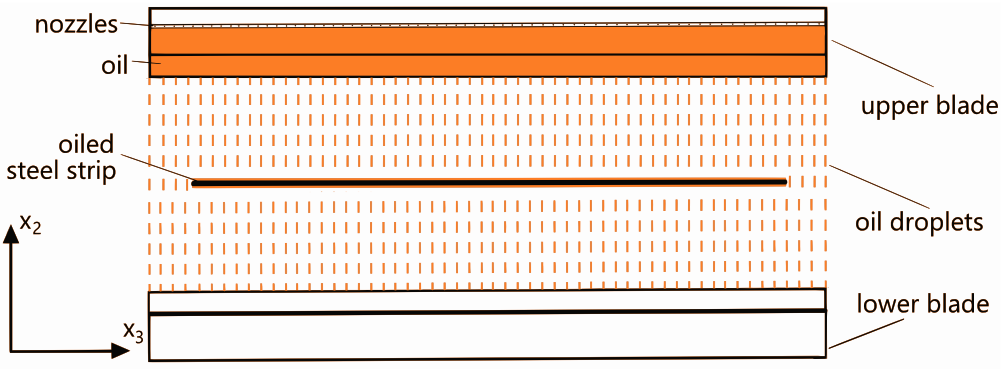

Figure 2.2: Front view of the electrostatic oiler blades.

As a consequence, the adhesion on the surface of the steel strips is high. This type of oil is known under the name dry lube. The oil is stocked in a tank and heated up at a temperature of about 30°C to lower the viscosity. Pumps deliver the oil to the blades. Each blade has two cavities. The oil is delivered through one of them while a heating fluid with a temperature of about 70°C is circulating through the other cavity. This is illustrated in Fig. 2.3. An oil temperature of 70°C is necessary to get the optimum atomization properties as shown in [9]. The heated oil flows through the nozzles and reaches the blade tip. Here, the oil is charged and atomized due to the high electric field strength. After the atomization, the oil droplets are accelerated by the electrostatic force towards the strip which is kept at ground potential.

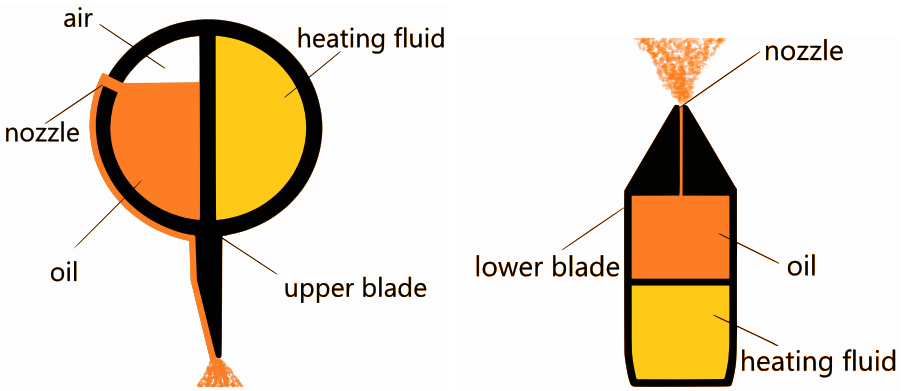

(a) Upper blade. (b) Lower blade.

Figure 2.3: Cross sections of the oiler blades.

The upper and the lower blade voltages are of opposite polarity and as a consequence, the droplets at the upper and the lower side are oppositely charged. Since the width of the strips is lower than the length of the blades as shown in Fig. 2.2, some of the oil droplets do not hit the strip. Droplets of the upper and the lower side electrically

neutralize each other and fall down into a bottom sump. As a consequence, loss of oil through the openings of the enclosure and overoiling of the strip edges are reduced [8].

The gutter shown in Fig. 2.1 can be swiveled between the idle position (dashed line) and the working position (solid line). In the idle position the gutter collects excess oil of the upper blade when the oiling process is stopped. This prevents excessive local oiling of the strip. The oil flows from the gutter into the bottom sump where the collected oil is pumped back into the tank. After the oiling process, the steel strips are coiled. Here, a redistribution of the oil film takes place.

Figure 2.4 shows the electrical equivalent circuit of the electrostatic oiling machine. The mentioned voltages $U_{\text{upper blade}}$ and $U_{\text{lower blade}}$ are generated by two voltage generators. $R_{\text{upper blade}}$ and $R_{\text{lower blade}}$ are the resistances of the blades and $R_{\text{upper oil spray}}$ and $R_{\text{lower oil spray}}$ are the non-linear resistances of the oil sprays depending, among others, on the voltages and the oil mass flow rates. R_{strip} and R_{contact} are the strip resistance and the contact resistance between the strip and the ground, respectively. The resistances $R_{1\ \text{leakage}}$, $R_{2\ \text{leakage}}$, and $R_{3\ \text{leakage}}$ represent the leakage currents due to corona discharges and metallic dust on the walls of the oiling machine. This metallic dust is produced during the previous skin passing process. The leakage current can be measured when the voltage is turned on while the oil mass flow rate is equal to zero.

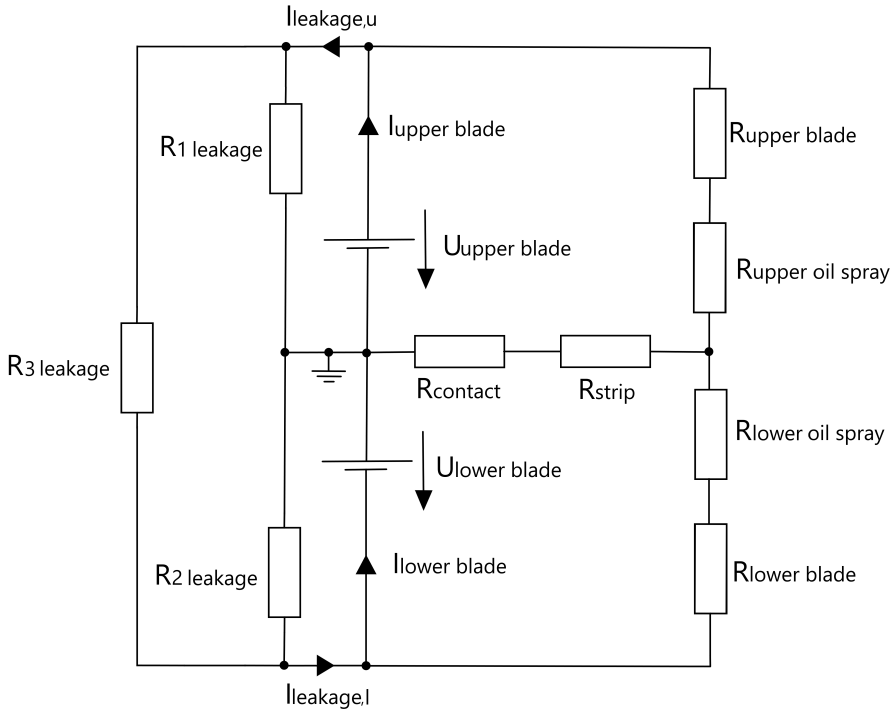

Figure 2.4: Electrical equivalent circuit of the electrostatic oiler.

3 Mathematical Model

This thesis deals with a numerical, two-dimensional, two-phase, steady-state model of the electrostatic oiler according to Fig. 2.1. A block diagram of the included physical quantities and the couplings is shown in Fig. 3.1. The model calculates the electric field, the air flow inside the enclosure of the electrostatic oiler and the droplet trajectories. The model of the air flow and the model of the droplets are coupled via the drag force acting on the droplets. The electric field model and the droplet model are coupled via the electrostatic force acting on the droplets and the charge carried by the droplets. The control variables of the electrostatic oiler are the voltages U between the blades and the strip, the oil mass flow rate Q, and the steel strip velocity v_{strip}. The current I and the initial droplet diameter d_{init} depend on the voltage, the oil mass flow rate, the blade geometry, the distance between the blade and the strip, and the oil properties. The current I is measured by default during the oiling process and is used as an additional input variable for the model as shown in Fig. 3.1. Moreover, the initial droplet diameter d_{init} is measured for the considered operating conditions and is also used as an input variable as shown in Fig. 3.1. Consequently, the spraying process can be simulated only for measured operating conditions. Nevertheless, the model fulfills the mentioned objectives. Basically, functions $I(U, Q, ...)$ and $d_{\text{init}}(U, Q, ...)$ could be modeled but this is beyond the scope of this thesis.

3.1 Theoretical Fundamentals

This section provides a brief overview of the theoretical background and the equations which are used for the model. For the sake of simplicity, the Einstein notation is used. For the sake of completeness, the full three-dimensional equations are considered, where $i, j = 1, 2, 3$.

3.1.1 Electric Field

The electric field which is generated by the charged oil droplets and the imposed voltage between the oiler blades and the strip is governed by Poisson's equation [10]

$$\frac{\partial^2 \varphi}{\partial x_i^2} = \frac{\rho_e}{\epsilon}, \tag{3.1}$$

where φ is the electric potential, ρ_e is the charge density and ϵ is the electrical permittivity of air. The imposed voltage is considered in the boundary conditions. The electric field $\boldsymbol{E}$ is calculated as follows

$$E_i = -\frac{\partial \varphi}{\partial x_i}. \tag{3.2}$$

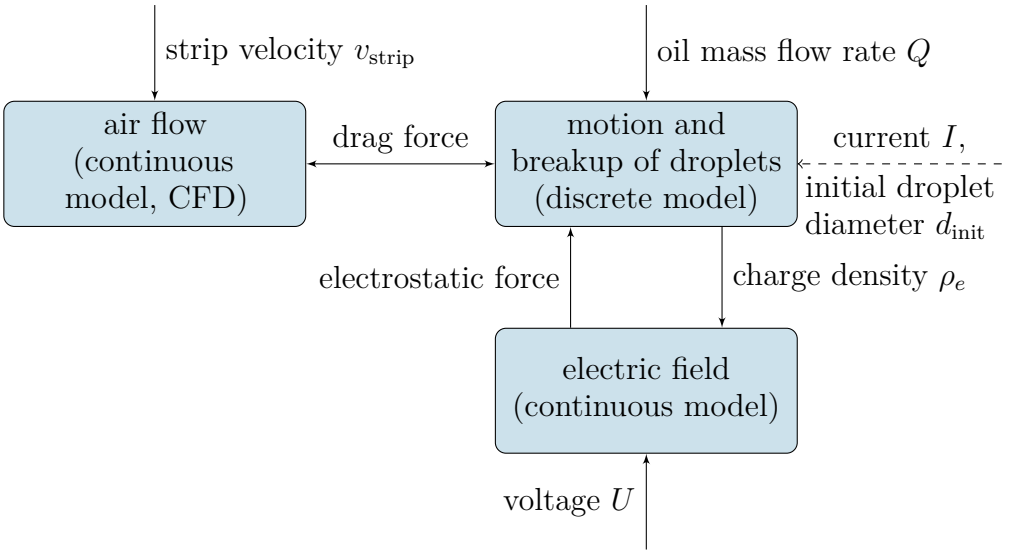

Figure 3.1: Block diagram of the model.

3.1.2 Air Flow

The air flow inside the oiling machine due to the movement of the oil droplets and the steel strip is calculated using the following equations.

Momentum and Mass Conservation Equation

The mass conservation also known as continuity equation reads as [11]

$$\frac{\partial \rho}{\partial t} + \frac{\partial}{\partial x_i}(\rho v_i) = 0, \tag{3.3}$$

where ρ is the mass density of air and $\boldsymbol{v}$ is the air flow velocity. The continuity equation states that the rate at which mass flows into a small volume is equal to the rate at which mass leaves plus the accumulation of mass in this volume. Under steady-state conditions, the time derivative vanishes and the continuity equation can be written as

$$\frac{\partial}{\partial x_i}(\rho v_i) = 0. \tag{3.4}$$

For incompressible flows

$$\frac{\partial v_i}{\partial x_i} = 0 \tag{3.5}$$

applies.

The momentum conservation equations also known as Navier-Stokes equations are [11]

$$\frac{\partial v_i}{\partial t} + v_j \frac{\partial v_i}{\partial x_j} = -\frac{1}{\rho}\frac{\partial p}{\partial x_i} + \nu \frac{\partial^2 v_i}{\partial x_j^2} - g\delta_{i,2} + a_i, \tag{3.6}$$

where p is the pressure, ν is the kinematic viscosity of air, g is the gravitational acceleration and $\boldsymbol{a}$ is an additional acceleration term due to the drag force acting on the droplets, according to (3.25). The Kronecker delta $\delta_{i,2}$ equals one for the x_2-direction in which the gravitational force is acting and is equal to zero for the other coordinates. The influence of the moving steel strip on the air flow is considered in the boundary conditions. The left hand side of (3.6) is the material derivative of the fluid velocity. The Navier-Stokes equations state that the material derivative of the fluid velocity depends on the pressure gradient $\frac{\partial p}{\partial x_i}$, on a friction term $\nu\frac{\partial^2 v_i}{\partial x_j^2}$ due to the viscosity of the fluid, on the gravitation, and on additional external body forces. Equation (3.6) shows the simplified Navier-Stokes equations for incompressible flows. This simplification is valid for fluids at Mach numbers $M = \frac{v}{c}$ of less than about 0.3 according to [11] where c is the speed of sound in the fluid. This condition is fulfilled for an electrostatic oiling machine.

If a steady-state flow is considered, the time derivative vanishes. Consequently, the Navier-Stokes equations read as

$$v_j\frac{\partial v_i}{\partial x_j} = -\frac{1}{\rho}\frac{\partial p}{\partial x_i} + \nu\frac{\partial^2 v_i}{\partial x_j^2} - g\delta_{i,2} + a_i. \tag{3.7}$$

Turbulence Model

Turbulent flows can be calculated by solving the Navier-Stokes equations (3.6). This is known as direct numerical simulation (DNS). In many practical cases, this leads to a prohibitive computational effort. However, the details of the turbulent flow are not required in most cases. Therefore, turbulence models are used where only the mean flow characteristics are calculated. There are different modeling strategies to reduce the computational effort. The most common strategy is the Reynolds decomposition that leads to Reynolds-averaged Navier-Stokes equations (RANS) [12].

Decomposition of the quantities of (3.6) into an time average $\bar{\bullet}$ and a fluctuating part $\bullet'$ leads to

$$\frac{\partial(\bar{v}_i + v_i')}{\partial t} + \left(\bar{v}_j + v_j'\right)\frac{\partial(\bar{v}_i + v_i')}{\partial x_j} = -\frac{1}{\rho}\frac{\partial(\bar{p} + p')}{\partial x_i} + \nu\frac{\partial^2(\bar{v}_i + v_i')}{\partial x_j^2} - g\delta_{i,2} + (\bar{a}_i + a_i'). \tag{3.8}$$

Time averaging leads to

$$\frac{\partial \bar{v}_i}{\partial t} + \bar{v}_j\frac{\partial \bar{v}_i}{\partial x_j} + \overline{v_j'\frac{\partial v_i'}{\partial x_j}} = -\frac{1}{\rho}\frac{\partial \bar{p}}{\partial x_i} + \nu\frac{\partial^2 \bar{v}_i}{\partial x_j^2} - g\delta_{i,2} + \bar{a}_i, \tag{3.9}$$

where the mean value of the fluctuating quantities is equal to zero.
Based on the assumption of an incompressible fluid, $\frac{\partial v_i}{\partial x_i} = \frac{\partial \bar{v}_i}{\partial x_i} + \frac{\partial v_i'}{\partial x_i} = 0$ and $\frac{\partial \bar{v}_i}{\partial x_i} = 0$, and thus also $\frac{\partial v_i'}{\partial x_i} = 0$ follow. Consequently, (3.9) can be written as

$$\frac{\partial \bar{v}_i}{\partial t} + \bar{v}_j\frac{\partial \bar{v}_i}{\partial x_j} + \frac{\overline{\partial v_i' v_j'}}{\partial x_j} = -\frac{1}{\rho}\frac{\partial \bar{p}}{\partial x_i} + \nu\frac{\partial^2 \bar{v}_i}{\partial x_j^2} - g\delta_{i,2} + \bar{a}_i. \tag{3.10}$$

Rearranging (3.10) and dropping the overbar on the mean quantities results in

$$\rho\frac{\partial v_i}{\partial t}+\rho v_j\frac{\partial v_i}{\partial x_j}=\frac{\partial}{\partial x_j}\left[-p\delta_{ij}+\rho\nu\frac{\partial v_i}{\partial x_j}-\rho\overline{v_i'v_j'}\right]-\rho g\delta_{i,2}+\rho a_i. \tag{3.11}$$

In the case of steady-state flows, we get

$$\rho v_j\frac{\partial v_i}{\partial x_j}=\frac{\partial}{\partial x_j}\left[-p\delta_{ij}+\mu\frac{\partial v_i}{\partial x_j}-\rho\overline{v_i'v_j'}\right]-\rho g\delta_{i,2}+\rho a_i. \tag{3.12}$$

One has to consider that the quantities are still mean values. The velocity fluctuations still appear in the nonlinear term $-\rho\overline{v_i'v_j'}$. This term is known as Reynolds stress and must be modeled in order to close (3.12). A common method employs the Boussinesq hypothesis to relate the Reynolds stresses to the mean velocity gradients [13], [14]

$$-\overline{v_i'v_j'}=2\nu_t S_{ij}-\frac{2}{3}k\delta_{ij}, \tag{3.13}$$

where ν_t is the turbulent viscosity, $k=\frac{1}{2}\overline{v_i'v_i'}$ is the turbulence kinetic energy (mean kinetic energy per unit mass associated with eddies in turbulent flow), and $S_{ij}=\frac{1}{2}\left(\frac{\partial v_i}{\partial x_j}+\frac{\partial v_j}{\partial x_i}\right)$ is the (i,j)-component of the strain rate tensor which describes the rate of change of the deformation of a fluid in the neighborhood of a certain point. This approach is used in the $k-\varepsilon$ model [15], [16] which is the most common model to simulate mean flow characteristics for turbulent flow conditions. The $k-\varepsilon$ model consists of two equations which describe the transport of the turbulence kinetic energy k and its dissipation rate (rate at which the turbulence kinetic energy is converted into heat by viscous forces) ε

$$\frac{\partial(\rho k)}{\partial t}+\frac{\partial(\rho k v_i)}{\partial x_i}=\frac{\partial}{\partial x_j}\left[\frac{\rho\nu_t}{\sigma_k}\frac{\partial k}{\partial x_j}\right]+2\rho\nu_t S_{ij}S_{ij}-\rho\varepsilon, \tag{3.14}$$

$$\frac{\partial(\rho\varepsilon)}{\partial t}+\frac{\partial(\rho\varepsilon v_i)}{\partial x_i}=\frac{\partial}{\partial x_j}\left[\frac{\rho\nu_t}{\sigma_\varepsilon}\frac{\partial\varepsilon}{\partial x_j}\right]+C_{1\varepsilon}\frac{\varepsilon}{k}2\rho\nu_t S_{ij}S_{ij}-C_{2\varepsilon}\rho\frac{\varepsilon^2}{k}, \tag{3.15}$$

where the constants σ_k, σ_ε, $C_{1\varepsilon}$, $C_{2\varepsilon}$ were determined by experiments. The terms in (3.14) and analog for (3.15) correspond to:
Rate of change of k + Transport of k by convection = Transport of k by diffusion + Rate of production of k − Rate of destruction of k, respectively.
The turbulent viscosity ν_t is calculated as

$$\nu_t=C_\mu\frac{k^2}{\varepsilon}. \tag{3.16}$$

With (3.14) – (3.16), the Reynolds stress (3.13) can be calculated and consequently, the RANS equations (3.12) can be solved.

Boundary Layer

The so-called no-slip condition requires the velocity of a fluid to match the velocity of a boundary surface. Here a transition layer arises in which the flow velocity changes rapidly from the velocity of the surface to the velocity of the surrounding fluid. The velocity profile $v(x_2)$ of a boundary layer is illustrated in Fig. 3.2, with the thickness of the boundary layer δ and the far field velocity v_0. To estimate the thickness of the boundary layer,

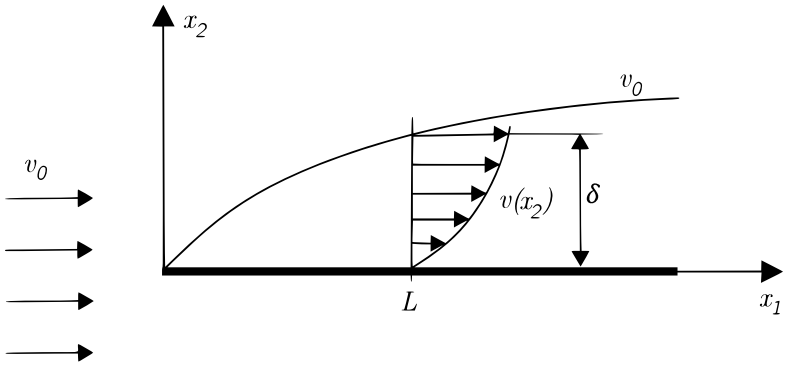

Figure 3.2: Boundary layer thickness δ.

the continuity equation (3.5) and the Navier-Stokes equations (3.7) for two-dimensional, steady-state, incompressible and laminar flow (neglecting the gravitation and additional body forces) are non-dimensionalized in the form: $\boldsymbol{x}^* = \frac{\boldsymbol{x}}{L}, \boldsymbol{v}^* = \frac{\boldsymbol{v}}{v_0}, p^* = \frac{p}{\rho v_0^2}$, with the dimensionless quantities $\bullet^*$ and appropriate reference quantities L, v_0 according to Fig. 3.2. The reference quantities are chosen such that $v_1^* \sim x_1^* \sim p^* \sim O(1)$, $x_2^* \sim O(\delta^*)$ applies. Scale analysis of the non-dimensionalized continuity equation and the non-dimensionalized x_1-component of the Navier-Stokes equations implies [17]

$$\underbrace{\frac{\partial v_1^*}{\partial x_1^*}}_{\sim 1} + \underbrace{\frac{\partial v_2^*}{\partial x_2^*}}_{\sim v_2^*/\delta^*} = 0 \implies v_2^* \sim \delta^*, \tag{3.17}$$

$$\underbrace{v_1^* \frac{\partial v_1^*}{\partial x_1^*}}_{\sim 1} + \underbrace{v_2^* \frac{\partial v_1^*}{\partial x_2^*}}_{\sim 1} = -\underbrace{\frac{\partial p^*}{\partial x_1^*}}_{\sim 1} + \frac{1}{Re}\left(\underbrace{\frac{\partial^2 v_1^*}{(\partial x_1^*)^2}}_{\sim 1} + \underbrace{\frac{\partial^2 v_1^*}{(\partial x_2^*)^2}}_{\sim 1/(\delta^*)^2} \right) \implies \delta^* \sim \frac{1}{\sqrt{Re}}, \tag{3.18}$$

where Re is the Reynolds number defined by

$$Re = \frac{v_0 L}{\nu}. \tag{3.19}$$

The Reynolds number can be interpreted as the ratio between the inertial forces and the viscous forces. The (dimensionalized) thickness of the boundary layer $\delta = \delta^* L$ at the

position L according to Fig. 3.2 can be approximated as follows

$$\delta \approx \frac{L}{\sqrt{Re}} = \sqrt{\frac{\nu L}{v_0}}. \tag{3.20}$$

In the case of a moving surface, v_0 is the difference between the strip velocity and the far field velocity of the surrounding air.

3.1.3 Oil Droplets

Equations of Motion

The droplet trajectories can be computed by two-times integration of the momentum balance

$$m_d \frac{d\boldsymbol{u}}{dt} = m_d \frac{\boldsymbol{v} - \boldsymbol{u}}{\tau} + m_d \boldsymbol{g} + q_d \boldsymbol{E}, \tag{3.21}$$

where the droplet inertia force $m_d \frac{d\boldsymbol{u}}{dt}$ is equated with the drag force $m_d \frac{\boldsymbol{v}-\boldsymbol{u}}{\tau}$, the gravitational force $m_d \boldsymbol{g}$ and the electrostatic force $q_d \boldsymbol{E}$. Here, m_d is the droplet mass, $\boldsymbol{u}$ is the droplet velocity, $\boldsymbol{v}$ is the velocity of the air in the vicinity of the droplet, q_d is the charge on the droplet, $\boldsymbol{E}$ is the electric field, and τ is the droplet relaxation time, which is the time constant of the dynamics of the droplet.
The droplet relaxation time is defined as [18]

$$\tau = \frac{\rho_d d^2}{18\mu} \frac{24}{C_D Re_d}, \tag{3.22}$$

where ρ_d is the density of the oil (the nominal value for the considered oil type can be found in Appendix A), d is the droplet diameter, $\mu = \rho\nu$ is the dynamic viscosity of air, C_D is a drag coefficient, and $Re_d = \frac{\rho d|\boldsymbol{v}-\boldsymbol{u}|}{\mu}$ is the Reynolds number.

The droplets are deformed due to the forces acting on them. This deformation is taken into account by a drag coefficient for non-spherical droplets according to [19] which is defined as

$$C_D = \frac{24}{Re_d}\left(1 + b_1 Re_d^{b_2}\right) + \frac{b_3 Re_d}{b_4 + Re_d}. \tag{3.23}$$

This drag coefficient depends on the shape factor $\frac{s}{S}$ which enters the expressions

$$\begin{aligned} b_1 &= \exp\left(2.3288 - 6.4581\left(\tfrac{s}{S}\right) + 2.4486\left(\tfrac{s}{S}\right)^2\right) \\ b_2 &= 0.0964 + 0.5565\left(\tfrac{s}{S}\right) \\ b_3 &= \exp\left(4.905 - 13.8944\left(\tfrac{s}{S}\right) + 18.4222\left(\tfrac{s}{S}\right)^2 - 10.2599\left(\tfrac{s}{S}\right)^3\right) \\ b_4 &= \exp\left(1.4681 + 12.2584\left(\tfrac{s}{S}\right) - 20.7322\left(\tfrac{s}{S}\right)^2 + 15.8855\left(\tfrac{s}{S}\right)^3\right). \end{aligned} \tag{3.24}$$

The shape factor is defined as the ratio between the surface area s of a sphere having the same volume as the droplet and the surface area S of the deformed droplet.

The air flow and the droplet trajectories are coupled via the drag force in both directions as shown in Fig. 3.1. The movement of the droplets leads to an acceleration $\boldsymbol{a}$ of the surrounding air (see (3.6)) in the form [20]

$$\boldsymbol{a} = \frac{1}{\rho V_{cell}} \sum_{k=1}^{N} \left(\frac{18 \mu C_D Re_d}{\rho_d d_k^2 24} (\boldsymbol{u}_k - \boldsymbol{v}) \right) Q_d \Delta t. \tag{3.25}$$

Here, V_{cell} is a small air volume with N droplets, $\boldsymbol{u}_k$ is the velocity of the k-th droplet within V_{cell}, Q_d is the mass flow rate of the droplets passing V_{cell}, and Δt is one time step of the calculation.

Rayleigh Limit

The theoretical maximum amount of charge that a droplet of diameter d can carry is described by the Rayleigh limit [21]

$$q_{\text{Rayleigh}} = 8\pi \sqrt{\epsilon_0 \gamma \left(\frac{d}{2} \right)^3}. \tag{3.26}$$

Here, γ is the surface tension (a typical value for the considered oil type can be found in Appendix A) and ϵ_0 is the permittivity of vacuum. This limit can be derived using perturbation methods as shown in [21]. If this limit is exceeded, the repelling forces between the charges, which are distributed on the droplet surface exceed the surface tension force, which holds the droplet together.

Let us consider a charged droplet with a diameter d whose charge q is equal to the Rayleigh limit

$$q = q_{\text{Rayleigh}} = 8\pi \sqrt{\epsilon_0 \gamma \left(\frac{d}{2} \right)^3}.$$

If the droplet breaks up into two equal droplets, each with a charge of $\frac{q}{2}$ and a diameter of $\frac{d}{\sqrt[3]{2}}$, a new charge limit

$$q_{\text{Rayleigh,child}} = 8\pi \sqrt{\epsilon_0 \gamma \left(\frac{d}{2\sqrt[3]{2}} \right)^3} = \frac{8\pi \sqrt{\epsilon_0 \gamma \left(\frac{d}{2} \right)^3}}{\sqrt{2}} = \frac{q}{\sqrt{2}}$$

for the child droplets follows. After the breakup, the charge of $\frac{q}{2}$ on the child droplets is below the new Rayleigh limit of $\frac{q}{\sqrt{2}}$. As a consequence, unstable droplets break up into child droplets as many times as necessary to fall below the Rayleigh limit.

However, this limit is valid only if the droplet liquid is a perfect conductor and if the droplet resides in vacuum without any external electric fields or external forces acting on the droplet. Different experimental studies, e.g. [22] and [23], have shown that the maximum droplet charge is below the Rayleigh limit for spray applications where high external electric fields are present, dielectric liquids are used, and a drag force is acting on the droplets. In [24], an extension to the Rayleigh limit is presented that incorporates

effects due to the permittivity of the droplets and due to external electric fields. It turns out that only 55% to 80% of the Rayleigh limit is reached in practice depending on the operating conditions. Hence, the corrected limit is

$$q_{\text{Limit}} = 8\pi K \sqrt{\epsilon_0 \gamma \left(\frac{d}{2}\right)^3}, \tag{3.27}$$

with a correction factor K between 0.55 and 0.8 which takes into account the electric field, the drag force, and the resistance and permittivity of the oil. The charge limit in relation to the droplet mass is

$$\frac{q_{\text{Limit}}}{m_d} = K \frac{6}{\rho_d} \sqrt{\epsilon_0 \gamma} \left(\frac{d}{2}\right)^{-\frac{3}{2}}. \tag{3.28}$$

Breakup Model

Droplets whose charge exceeds the Rayleigh limit break up into smaller droplets. This process is also called secondary breakup while a primary breakup describes the breakup of a fluid into droplets. There are different (secondary) breakup models like the Taylor Analogy Breakup model [25], the Wave Breakup model [26], the Kelvin-Helmholtz-Rayleigh-Taylor (KHRT) model [27] or the Stochastic Secondary Droplet (SSD) model [28]. Each model is suitable for a different range of Weber numbers. The Weber number is defined as [29]

$$We = \frac{\rho |\boldsymbol{v} - \boldsymbol{u}|^2 \frac{d}{2}}{\gamma}. \tag{3.29}$$

This dimensionless number indicates the relative importance of a fluid's inertia in comparison with its surface tension. Generally, the mentioned models do not capture the additional destabilizing effect of electrical charges on the droplets. However, the SSD model is well suited to approximate this effect. The SSD model predicts that droplets larger than a critical diameter [28]

$$d_{\text{cr}} = 2 \frac{We_{\text{cr}} \gamma}{\rho |\boldsymbol{v} - \boldsymbol{u}|^2}, \tag{3.30}$$

will break up. We_{cr} is the critical Weber number. From (3.27), a maximum droplet diameter that is stable for a given charge q follows in the form

$$d_{\text{Limit}} = 2 \left(\left(\frac{q}{8\pi K}\right)^2 \frac{1}{\epsilon_0 \gamma} \right)^{\frac{1}{3}}. \tag{3.31}$$

According to (3.31) a droplet breakup is mainly caused by the charges on the droplet and by the drag force (considered in K), which depends on the relative velocity between the droplets and the surrounding air as stated in (3.21). In contrast, the breakup model (3.30) only considers the relative velocity. It is tried to predict the diameters of the child droplets after the breakup process using (3.30). This is done by selecting We_{cr} in (3.30)

such that $d_{\mathrm{cr}} = d_{\mathrm{Limit}}$ applies. The evaluation of We_{cr} is shown in Chapter 5.

The second parameter of the SSD model is the breakup time which is defined as [28]

$$t_{\mathrm{bu}} = B\sqrt{\frac{\rho_d}{\rho}}\frac{\frac{d}{2}}{|\boldsymbol{v}-\boldsymbol{u}|}, \tag{3.32}$$

where B is a constant. The breakup time corresponds to the duration of a single droplet breakup. The evaluation of B is also shown in Chapter 5.

The diameters of the child droplets are are normal distributed in logarithmic terms [20], [28]

$$T(x) = \frac{1}{\sqrt{2\pi\sigma^2}}\exp\left[\frac{-(x-x_0-\xi)^2}{2\sigma^2}\right], \tag{3.33}$$

where $x = \ln(\frac{d}{2})$ and $x_0 = \ln(\frac{d_0}{2})$ with the diameter d_0 of the parent droplet. The child droplets are smaller than the parent droplet by a factor of $\exp(\xi)$ on average. Under the assumption that the droplets typically break up into two child droplets of the same size, $\exp(\xi) = \frac{1}{\sqrt[3]{2}}$ and consequently $\xi = -0.231$ follows. The parameter σ^2 is the variance of the diameter distribution, again in logarithmic terms. According to [28], the variance is calculated as $\sigma^2 = -0.1\ln\left(\frac{We_{\mathrm{cr}}}{We}\right)$. Consequently, the diameter distribution is broad for high Weber numbers We (3.29) compared to the critical Weber number We_{cr} when a breakup occurs.

3.2 Numerical Model Implemented in ANSYS Fluent

The presented model describes a nonlinear, multiphysics problem with two phases and distributed parameters. Due to the high complexity of the corresponding equations, a numerical solution method has to be employed. For this purpose, the computational fluid dynamics software ANSYS Fluent [30] is used. Fluent uses the finite volume method to solve the equations. Fluent does not provide a solution for the electrostatic field by default. However, user-defined scalar transport equations and user-defined functions can be used for this purpose. An advantage of Fluent is that it includes a comprehensive discrete phase model (DPM) to describe the droplet trajectories and the breakup process. Furthermore, there is the possibility to extend the DPM by user-defined functions.

A flow chart of the implemented iterative solution method is shown in Fig. 3.3. In the first step, all the quantities are initialized. Then, an initial electric field due to the imposed voltage between the blade and the strip is calculated. For this, (3.1) and (3.2) are solved where the imposed voltage enters the boundary conditions. In addition, the charge density ρ_e is set to zero for this initial iteration because the trajectories of the charged droplets are unknown.

In the next step, the droplet trajectories are calculated. For this, the droplets (or sets of droplets, so-called parcels) are tracked where (3.21) – (3.24) are solved for the initial guess of the electric field. The electrostatic force acting on the droplets is included

as user-defined function. The droplet charge to mass ratio used for the evaluation of the electrostatic force is calculated as $\frac{q_d}{m_d} = \frac{I}{Q}$ where I is the measured electric current ($I_{\text{blade}} - I_{\text{leakage}}$ according to Fig. 2.4) and Q is the measured oil mass flow rate. The droplets break up according to (3.30), (3.32), and (3.33).

The droplet trajectories are used to compute the charge density as $\rho_e = \frac{q_d}{m_d} C$, with the droplet mass concentration C (oil mass per unit volume) which can be acquired from the Fluent solver.

In the next step, the airflow due to the movement of the droplets and the steel strip is calculated according to (3.5), (3.12) - (3.16) and (3.25). The no-slip boundary condition is specified for the surface of the steel strip and the walls of the enclosure. A constant pressure boundary condition is used for the outlets of the enclosure.

Then, the electric field is recalculated under consideration of the charge density ρ_e. These steps are iteratively repeated until the change of the air flow velocity and the change of the pressure from iteration to iteration is less than a certain threshold.

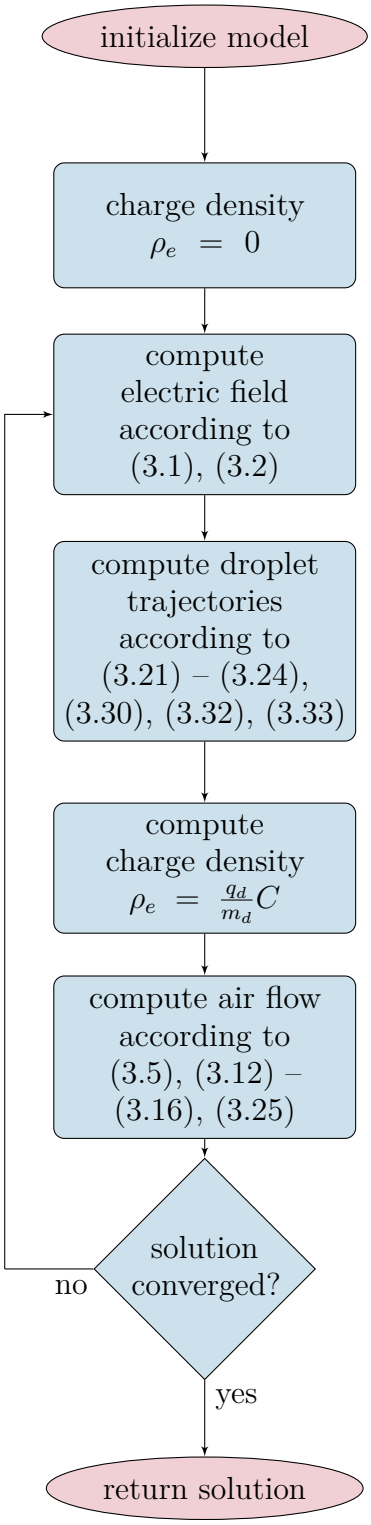

Figure 3.3: Flow chart of the numerical model implemented in ANSYS Fluent.

4 Measurements

This chapter describes the measurements that were made to create and validate the model. The quantities listed in Tab. 4.1 are recorded by default during the oiling process and were used for this work.

Quantity	Symbol
Strip speed	v_{strip}
Blade voltage	U
Blade current	I
Oil mass flow rate	Q
Blade to strip distance	$l_{\text{blade - strip}}$

Table 4.1: Recorded data.

Moreover, the oil droplet velocities and diameters were measured using the standard digital camera Nikon Coolpix P520. Sensors cannot be located inside the electrostatic oiler due to the high voltage. Therefore, the images were captured through a small inspection window. Figure 4.1 shows a picture of the oil spray at the upper blade. Lengths can be approximately evaluated by counting of pixels and conversion with the scaling factor $28\frac{\mu\text{m}}{\text{px}}$. The shutter time of the camera is $T_s = 0.5\text{ms}$. The velocities and diameters of the droplets are calculated from the pictures according to Figs. 4.2 and 4.3.

The quantities were measured at the positions A and B indicated in Figs. 4.1 and 4.4 and for different operating conditions. The uncertainty of the velocity measurement is mainly caused by the uncertainty of the shutter time, which is about 20% of the nominal value according to [31]. An uncertainty (reading accuracy) of 1.5 pixels is assumed for the diameter measurement. The perspective error can be neglected compared to the mentioned uncertainties.

It was found that the oil is not atomized right at the blade tip but oil jets are formed as shown in Fig. 4.5. These jets leave the blade at the tip of cones as illustrated in Fig. 4.6. These cones are also known as Taylor cones [32]. The formation of liquid jets due to high voltage is well known and described e.g. in [32–39]. However, the formation is described only for single oil jets where the liquid is supplied via a capillary tube as outlined in Fig. 4.6. In addition, the forces acting on the cone, according to [37], are depicted. Figure 4.5 shows several jets side by side along the oiler blade. After a few centimeters, the jets break up into droplets as shown in Fig. 4.5. Furthermore, it was observed that the diameters of the jets decrease with increasing blade voltage and

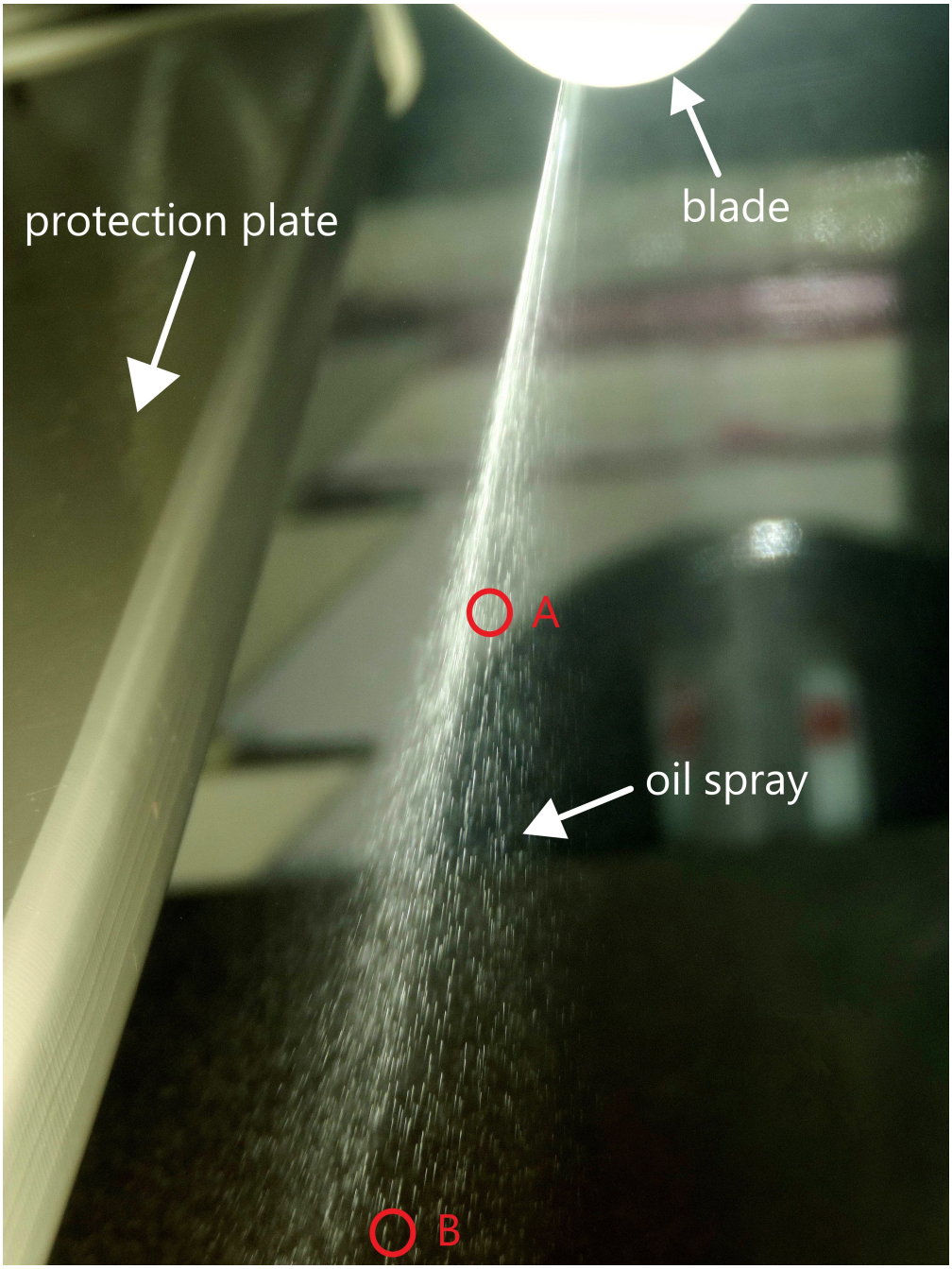

Figure 4.1: Oil spray at the upper blade with the positions A and B where the droplet velocity and diameter is evaluated.

consequently with increasing charge. This is for the same reason as described for the droplets in Section 3.1.3. For a given oil mass flow rate, the distance between the jets

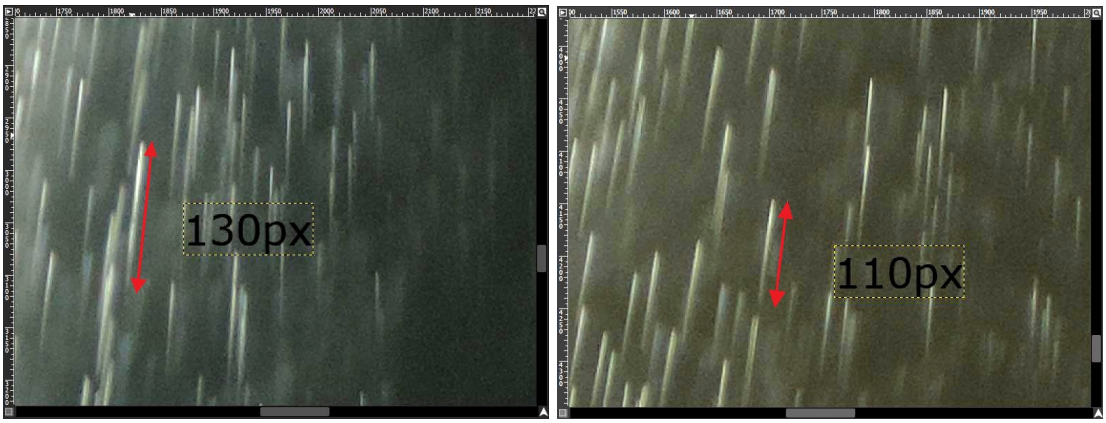

(a) Position A. (b) Position B.

Figure 4.2: Droplet velocity measurement.

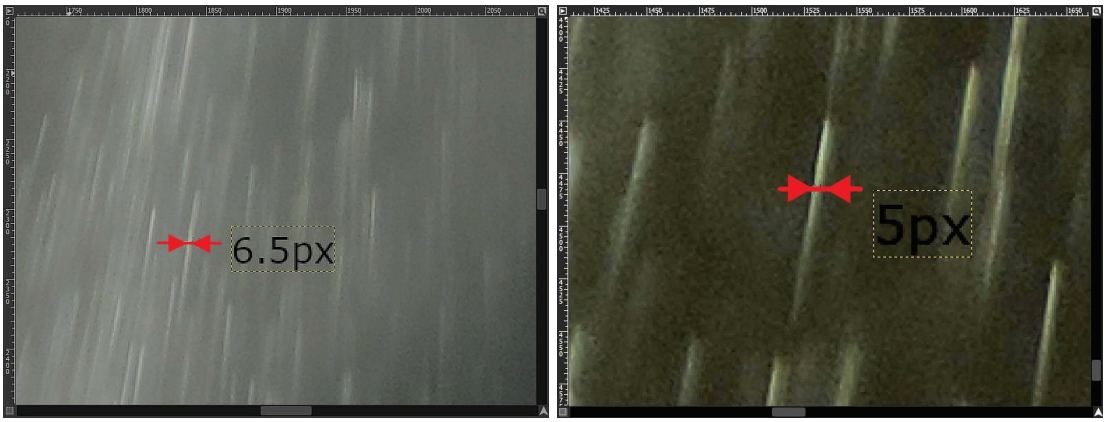

(a) Position A. (b) Position B.

Figure 4.3: Droplet diameter measurement.

decreases with decreasing jet diameters. The formation of stable oil cones and oil jets requires a minimum voltage according to [34] and [40]. The imposed voltage at the lower blade has to be higher than the voltage at the upper blade because the gravity acts against the formation of the cones at the lower side. There is also an upper blade voltage limit due to flashovers. This limit depends on the metallic dust inside the oiling machine. Due to the complexity of the breakup of the oil jets into droplets (primary breakup), the oil jets are approximated by droplets with the same diameter (d_{init}) starting at the blade tip. The resulting error is small because of the small lengths of the jets.

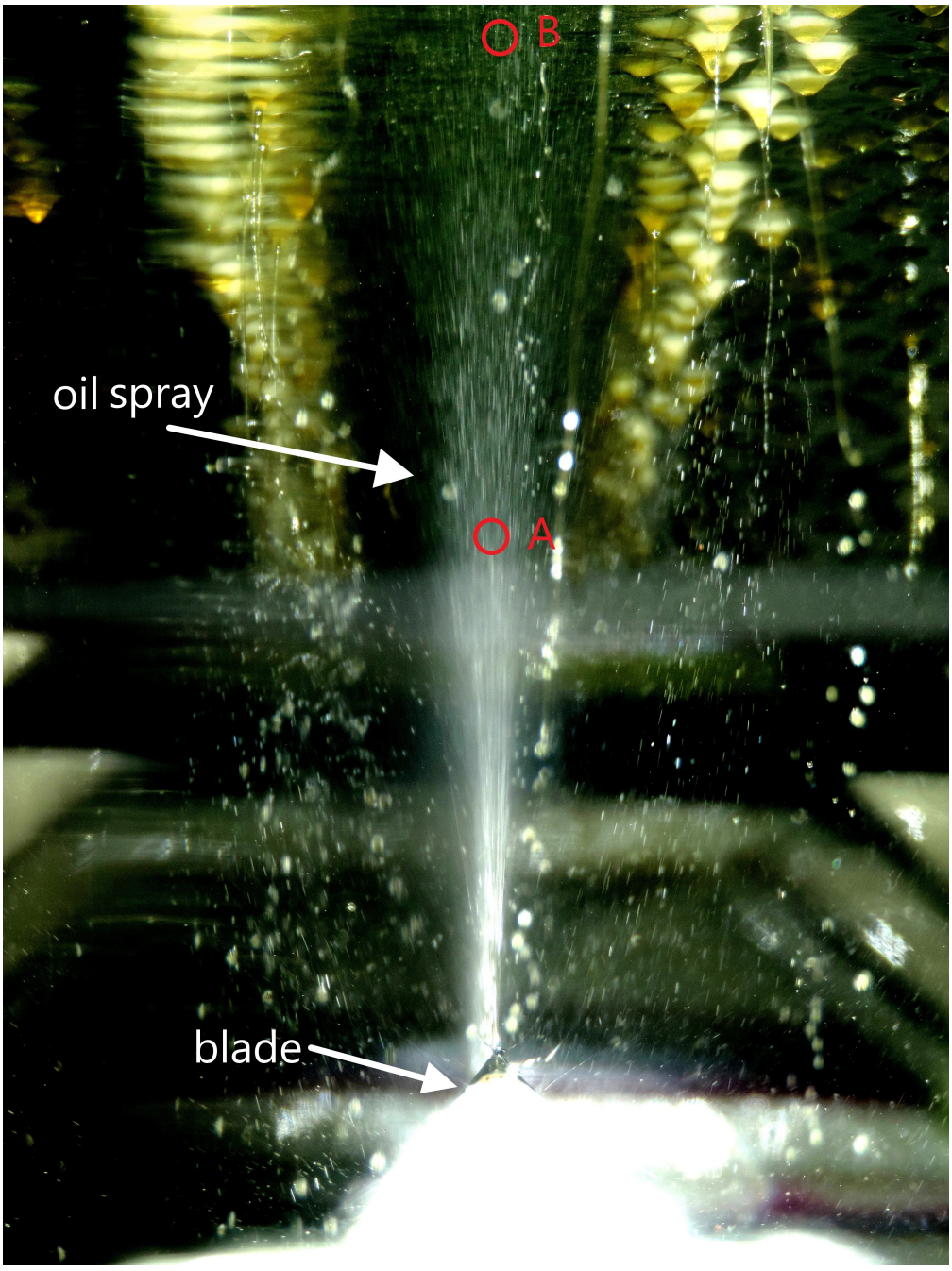

Figure 4.4: Oil spray at the lower blade with the positions A and B where the droplet velocity and diameter is evaluated.

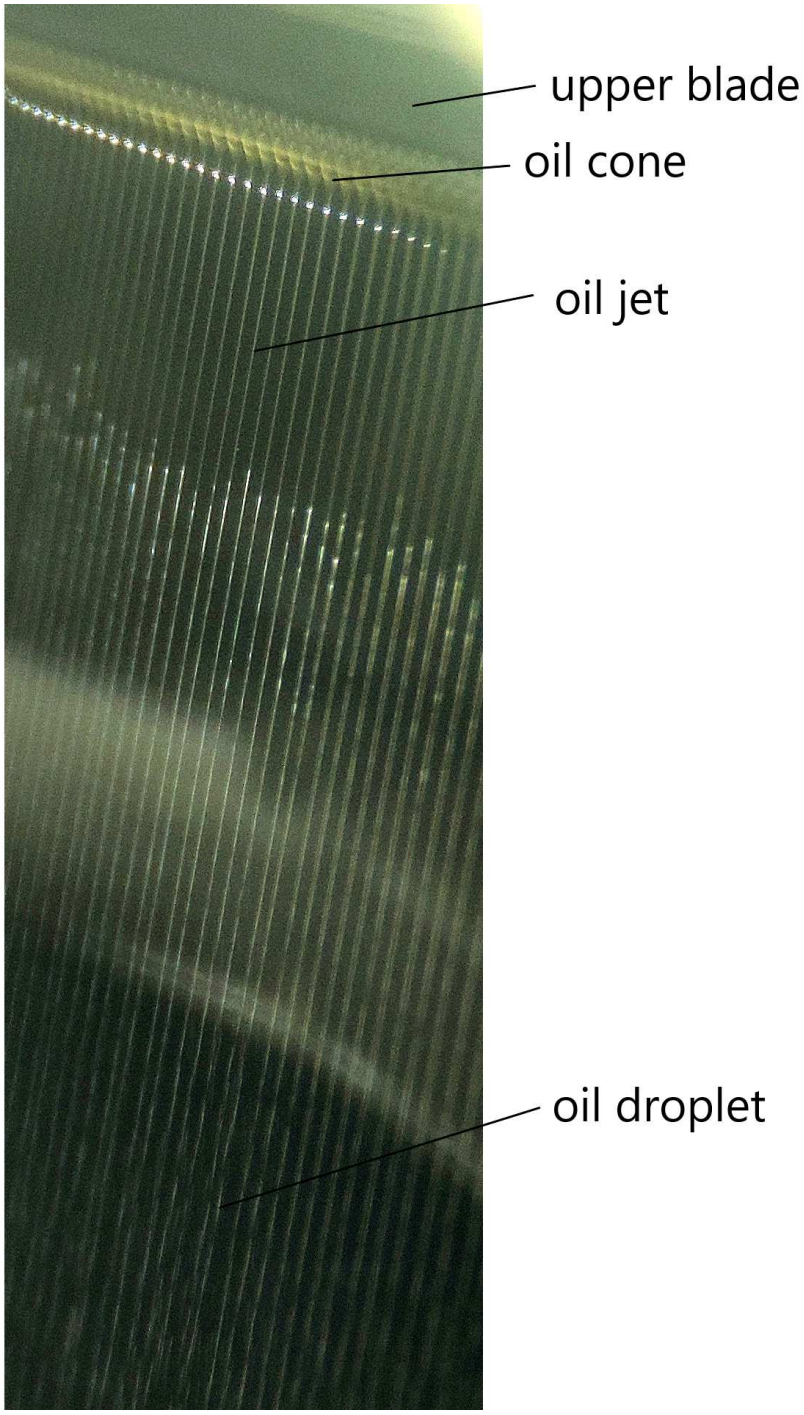

Figure 4.5: Oil jets starting at the blade tip.

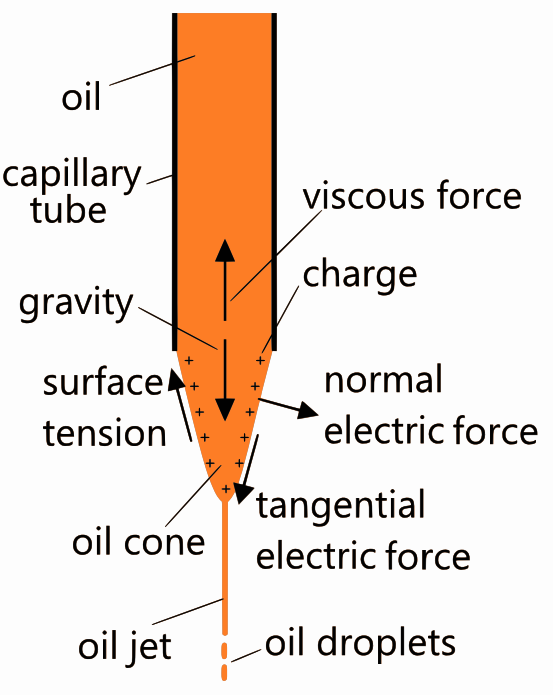

Figure 4.6: Oil jet starting at the tip of a cone [37].

5 Model Validation

In this chapter, the unknown parameters of the model are identified and subsquently the model results are compared with measurements. Furthermore, some conclusions from the simulations are summarized.

5.1 Parameter Optimization

It is not possible to identify all the unknown model parameters of Chapter 3 using the measurements of Chapter 4. Consequently, most parameters are set to their nominal values and only the unknown parameters, i.e. the droplet shape factor $\frac{s}{S}$ in (3.24), the critical Weber number We_{cr} in (3.30), and the breakup time factor B in (3.32), are estimated. For this purpose, the parameter vector $\boldsymbol{p}^T = [\frac{s}{S}, We_{\mathrm{cr}}, B]$ is defined. The parameters are estimated by minimizing the differences between the simulation results and the measurements, using the Optimization Toolbox of MATLAB. The measurements are merged into the vector $\boldsymbol{y}^T_{\mathrm{measured}} = [|\boldsymbol{u}_A|, |\boldsymbol{u}_B|, d_A, d_B]$, where $\boldsymbol{u}_A$, $\boldsymbol{u}_B$ are the droplet velocities and d_A, d_B are the droplet diameters at the positions A and B according to Figs. 4.1 and 4.4. The optimization problem reads as

$$\begin{aligned} \min_{\boldsymbol{p}\in\mathbb{R}^3} f(\boldsymbol{p}) &= \sum_{i=1}^{4} \left| \frac{(y_{i,\mathrm{simulated}}(\boldsymbol{p}) - y_{i,\mathrm{measured}})}{y_{i,\mathrm{measured}}} \right| \\ \text{s.t. } & \text{ANSYS Fluent model Fig. 3.3} \\ & p_1 - 1 \leq 0 \\ & -p_1 \leq 0 \\ & -p_2 \leq 0 \\ & -p_3 \leq 0. \end{aligned} \tag{5.1}$$

The cost function $f(\boldsymbol{p})$ is the sum of the normalized absolute differences between the simulated and the measured values.

The two contour plots in Fig. 5.1 give an idea of the location of the optimum. Subfigure 5.1(a) shows the cost function for various droplet shape factors and critical Weber numbers while the breakup time factor is held constant. In Subfigure 5.1(b), the critical Weber number and the breakup time parameter are varied.
According to these contour plots, a reasonable starting point for an iterative search for a minimum of $f(\boldsymbol{p})$ is chosen. The exact optimum is calculated with the function *fminsearch* of the MATLAB Optimitzation Toolbox [41]. This function uses the simplex search method of Lagarias et al. [42], which shows a good convergence behavior for the considered problem as presented in Fig. 5.2.
The optimum parameter values for the operating conditions $U = 50\mathrm{kV}$, $I = 23\mu\mathrm{A}$,

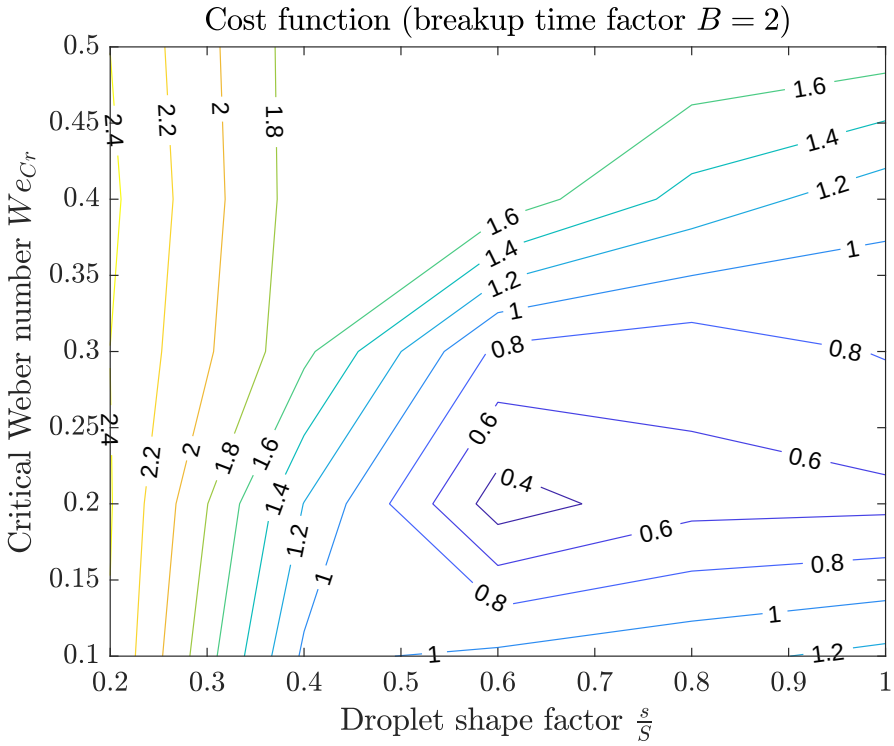

(a) Constant breakup time factor $B = 2$.

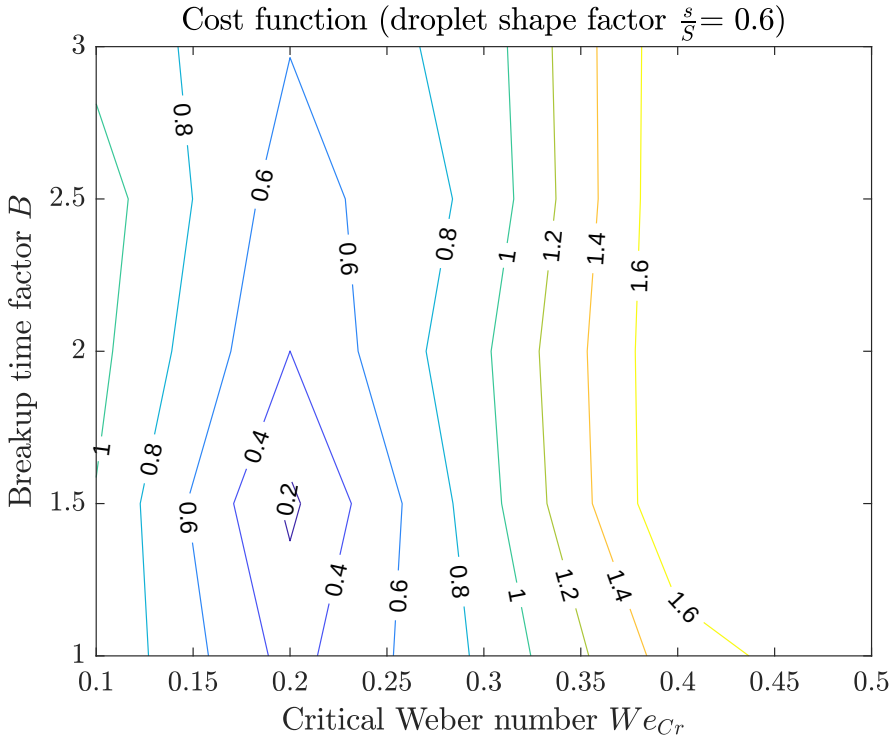

(b) Constant droplet shape factor $\frac{s}{S} = 0.6$.

Figure 5.1: Contour plots of the cost function $f(\boldsymbol{p})$.

$Q = 6.5\text{gs}^{-1}$, $d_{\text{init}} = 280\mu\text{m}$, and the distance between the blade and the strip $l_{\text{blade-strip}} = 305\text{mm}$ at the upper blade are

$$\boldsymbol{p}_{\text{opt}}^T = \begin{bmatrix} \frac{s}{S} \\ We_{cr} \\ B \end{bmatrix}_{opt} = \begin{bmatrix} 0.66 \\ 0.24 \\ 2.05 \end{bmatrix}. \tag{5.2}$$

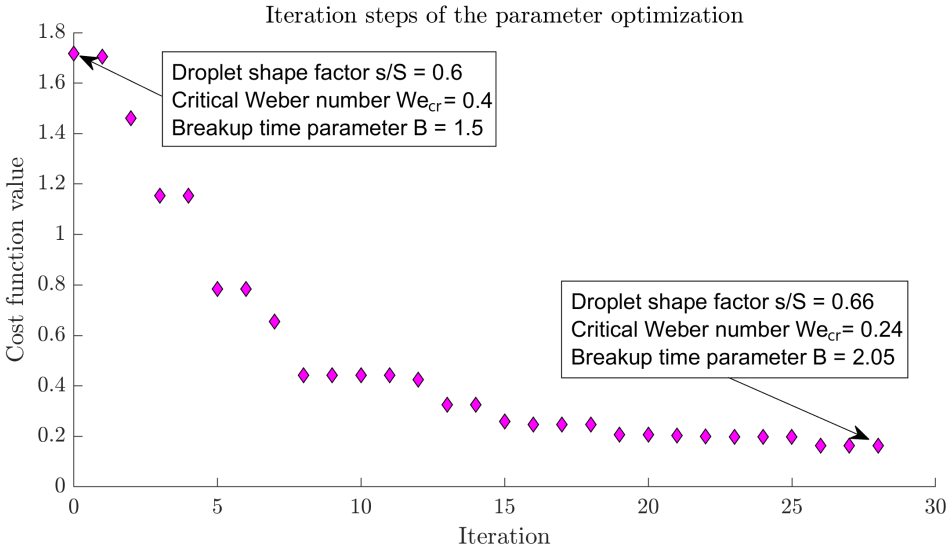

Figure 5.2: Iteration steps of the parameter optimization.

5.2 Comparison of Measurements and Simulations

The optimized parameter values (5.2) are used to simulate the oiling process under different conditions at the upper and the lower blade. Figures 5.3 to 5.5 show qualitative comparisons of the actual and the simulated oil trajectories for different operating conditions. These figures show a good agreement between simulation results and measurements. For these results, a droplet breakup model is necessary as shown in Figure A.1. Furthermore, a comparison of Fig. 5.3 and 5.4 shows the dependence of the oil spray on the voltage level.

Table 5.1 compares the measured and the simulated oil droplet velocities and diameters at the positions A and B according to Figs. 4.1 and 4.4, again for different operating conditions.

The simulation results are in good agreement with the measured values for the considered operating conditions. Therefore, one set of parameters (5.2) suffices to describe the oiling process with reasonable accuracy.

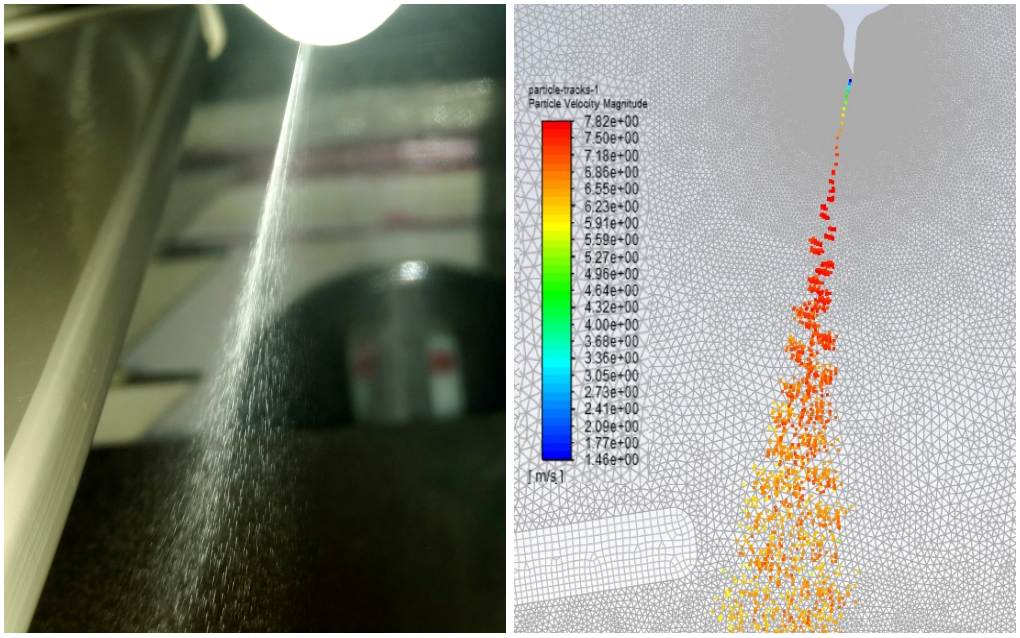

(a) Photo (b) Simulation

Figure 5.3: Actual vs. simulated oil trajectories at the upper blade at 50kV.

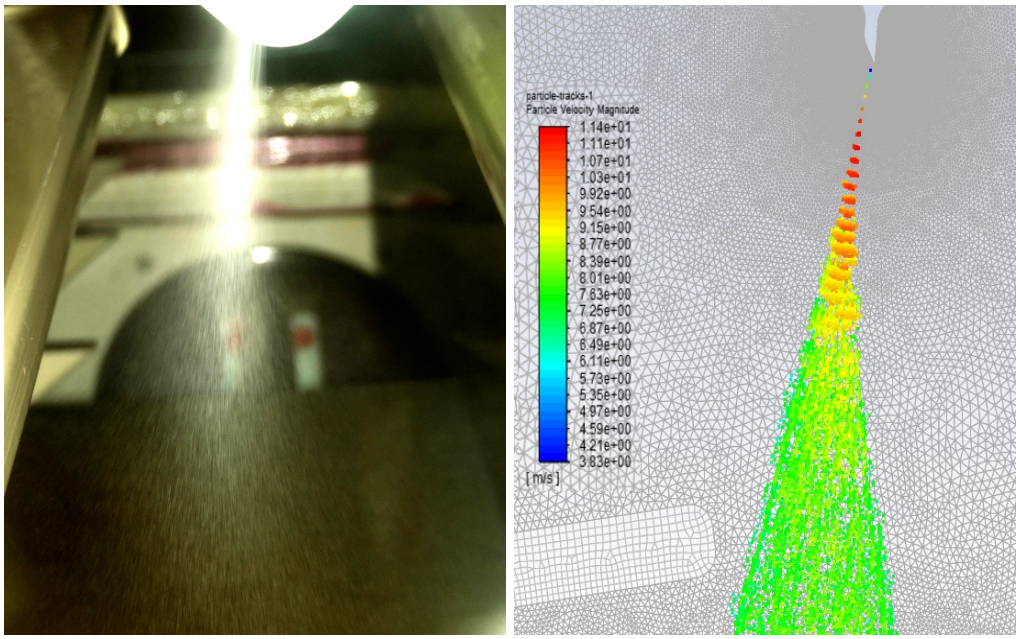

(a) Photo (b) Simulation

Figure 5.4: Actual vs. simulated oil trajectories at the upper blade at 105kV.

Quantity	Position	Measured	Simulated	Conditions (measured)
		Upper blade		
Velocity (m/s)	A	7.3	7.4	$U = 50\text{kV}$
	B	6.4	6.4	$I = 23\mu\text{A}$
Diameter (μm)	A	185	190	$Q = 6.5\text{gs}^{-1}$
	B	140	160	$d_{\text{init}} = 280\mu\text{m}$
Velocity (m/s)	A	9.3	9.0	$U = 75\text{kV}$
	B	8.3	7.9	$I = 29\mu\text{A}$
Diameter (μm)	A	140	135	$Q = 6.8\text{gs}^{-1}$
	B	125	130	$d_{\text{init}} = 190\mu\text{m}$
Velocity (m/s)	A	10.2	10.0	$U = 105\text{kV}$
	B	8.5	8.8	$I = 36\mu\text{A}$
Diameter (μm)	A	110	95	$Q = 6.7\text{gs}^{-1}$
	B	100	90	$d_{\text{init}} = 140\mu\text{m}$
		Lower blade		
Velocity (m/s)	A	7.7	8.1	$U = -50\text{kV}$
	B	6.8	7.4	$I = -20\mu\text{A}$
Diameter (μm)	A	130	125	$Q = 4.1\text{gs}^{-1}$
	B	105	97	$d_{\text{init}} = 320\mu\text{m}$
Velocity (m/s)	A	8.6	9.2	$U = -75\text{kV}$
	B	7.4	7.8	$I = -52\mu\text{A}$
Diameter (μm)	A	96	100	$Q = 9.3\text{gs}^{-1}$
	B	80	90	$d_{\text{init}} = 250\mu\text{m}$

Table 5.1: Comparison of measured and simulated values. Measurement uncertainty according to Chapter 4, positions according to Figs. 4.1 and 4.4, $l_{\text{upper blade}-\text{strip}} = 305\text{mm}$, $l_{\text{lower blade}-\text{strip}} = 135\text{mm}$, oil properties according to Appendix A.

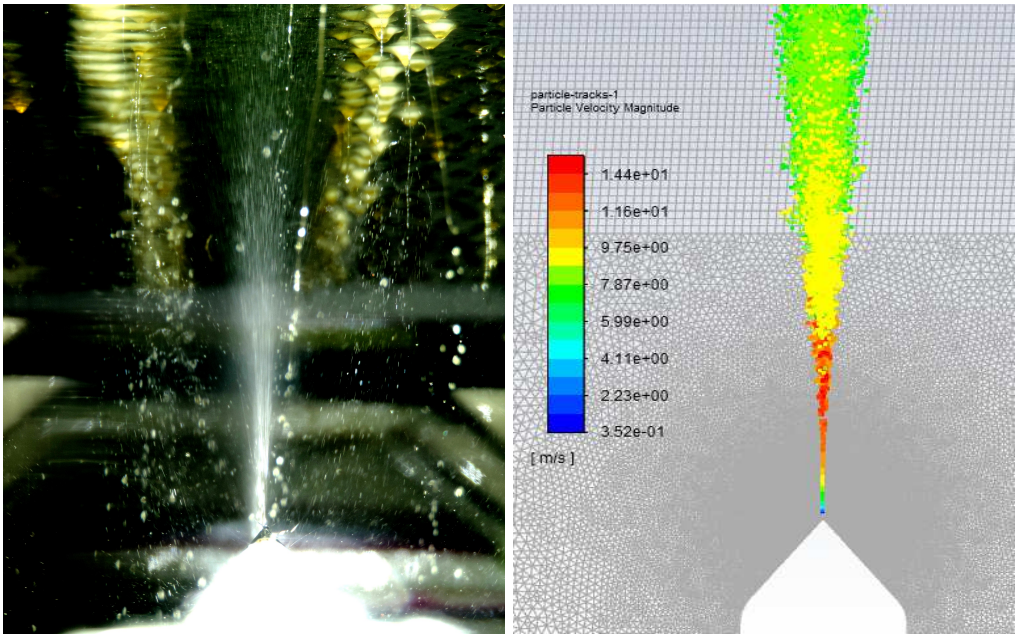

(a) Photo (b) Simulation

Figure 5.5: Actual vs. simulated oil trajectories at the lower blade at 75kV.

5.3 Plausibility Check Using the Rayleigh Limit

In this section, the obtained results are checked for plausibility based on the Rayleigh limit defined in Section 3.1.3. From (3.28), the limit for stable droplet diameters follows in the form

$$d_{\text{Limit}} = 2\left(\frac{\frac{I}{Q}\rho_d}{6K\sqrt{\epsilon_0\gamma}}\right)^{-\frac{2}{3}}, \tag{5.3}$$

for a given charge on the droplets. The charge to mass ratio is calculated as $\frac{q_d}{m_d} = \frac{I}{Q}$. Values for the density ρ_d and the surface tension γ can be found in Appendix A. The value d_{Limit} corresponds to the maximum possible droplet diameter which is stable for a given electric charge on the droplet. This means that all the droplets have to break up into child droplets with a diameter equal to this limit or smaller

$$d \leq d_{\text{Limit}}. \tag{5.4}$$

Table 5.2 compares the calculated diameter limits with the measured maximum droplet diameters at the position B according to Fig. 4.1 and 4.4. As expected, all measured droplet diameters are below d_{Limit} at position B.

Droplet diameter d(μm)		
d_{Limit}	Measured	Conditions (measured)
Upper Blade		
152	140	$U = 50\text{kV}$ $I = 23\mu\text{A}$ $Q = 6.5\text{gs}^{-1}$ $d_{\text{init}} = 280\mu\text{m}$
134	125	$U = 75\text{kV}$ $I = 29\mu\text{A}$ $Q = 6.8\text{gs}^{-1}$ $d_{\text{init}} = 190\mu\text{m}$
115	100	$U = 105\text{kV}$ $I = 36\mu\text{A}$ $Q = 6.7\text{gs}^{-1}$ $d_{\text{init}} = 140\mu\text{m}$
Lower Blade		
122	105	$U = -50\text{kV}$ $I = -20\mu\text{A}$ $Q = 4.1\text{gs}^{-1}$ $d_{\text{init}} = 320\mu\text{m}$
112	80	$U = -75\text{kV}$ $I = -52\mu\text{A}$ $Q = 9.3\text{gs}^{-1}$ $d_{\text{init}} = 250\mu\text{m}$

Table 5.2: Comparison of calculated droplet diameter limits (5.3) (for $K = 0.7$) and measured maximum droplet diameters at position B according to Figs. 4.1 and 4.4, measurement uncertainty according to Chapter 4, $l_{\text{upper blade}-\text{strip}} = 305\text{mm}$, $l_{\text{lower blade}-\text{strip}} = 135\text{mm}$, oil properties according to Appendix A.

5.4 Further Simulation Results

This section summarizes the main simulation results. Figure 5.6 shows the electric potential according to (3.1) with the boundary conditions $\varphi_{\text{blade}} = 76\text{kV}, \varphi_{\text{strip}} = 0\text{V}$. In Subfigure 5.6(a), the oil mass flow rate per meter is $\tilde{Q} = 0\text{g(sm)}^{-1}$, in Subfigure 5.6(b) $\tilde{Q} = 1.5\text{g(sm)}^{-1}$. A comparison of these figures shows the influence of the charged droplets on the electric potential.

Figure 5.7 presents the electric field calculated by (3.2). The field vectors are perpendicular to the equipotential lines. The field strength has a maximum around the blade tip.

Figure 5.8 shows the air flow velocity due to the movement of the oil droplets and the steel strip. The strip is stationary in Subfigure 5.8(a) and moving at the maximum speed in Subfigure 5.8(b). Subfigure 5.8(b) also shows the thin boundary layer near the strip.

The oil droplet velocities and diameters are shown in Fig. 5.9 for $v_{\text{strip}} = 5ms^{-1}$. The trajectories are practically not influenced by the boundary layer flow due to the low thickness of this layer and the high droplet speed.

Figure 5.10 compared to Fig. 5.9 demonstrates the influence of the voltage on the oil droplet trajectories. For higher voltages, the droplet velocity increases because of the increased electrostatic force. The droplet diameters decrease because the critical breakup diameter decreases with increasing velocity according to (3.30). Furthermore, the oil spray is widened because the oil carries more charge with increasing voltage. This may be inferred from increasing the $\frac{I}{Q}$-ratio according to Tab. 5.1.

Figure 5.11 shows the influence of the oil mass flow rate Q on the droplet trajectories. The oil spray is widened when Q is increased due to the additional space charge.

The electric field of the lower blade is shown in Fig. 5.12 for two different distances between the blade and the strip. Clearly, the field strength increases when this distance is reduced and, as a consequence, the droplet velocity increases as shown in Fig. 5.13.

Figure 5.14 shows that the droplets travel approximately $t_{\text{travel}} = 43\text{ms}$ from the upper blade to the strip.

Furthermore, the forces acting on the droplets are evaluated at the positions A, B, and C illustrated in Fig. 5.15. According to the equations of motion (3.21), there are three types of forces acting on the droplets. These are the drag force, the gravitational force, and the electrostatic force. The simulation results are summarized in Tab. 5.3. At all three points, the gravitational force is at least one decade smaller than the other forces. Around the blade tip (position A), where the droplets are strongly accelerated, the electrostatic force is more than one decade higher compared to the drag force. Further away from the blade, the drag force exceeds the electrostatic force and the droplet velocity decreases. This can also be seen in Figs. 5.9 – 5.11 and 5.13.

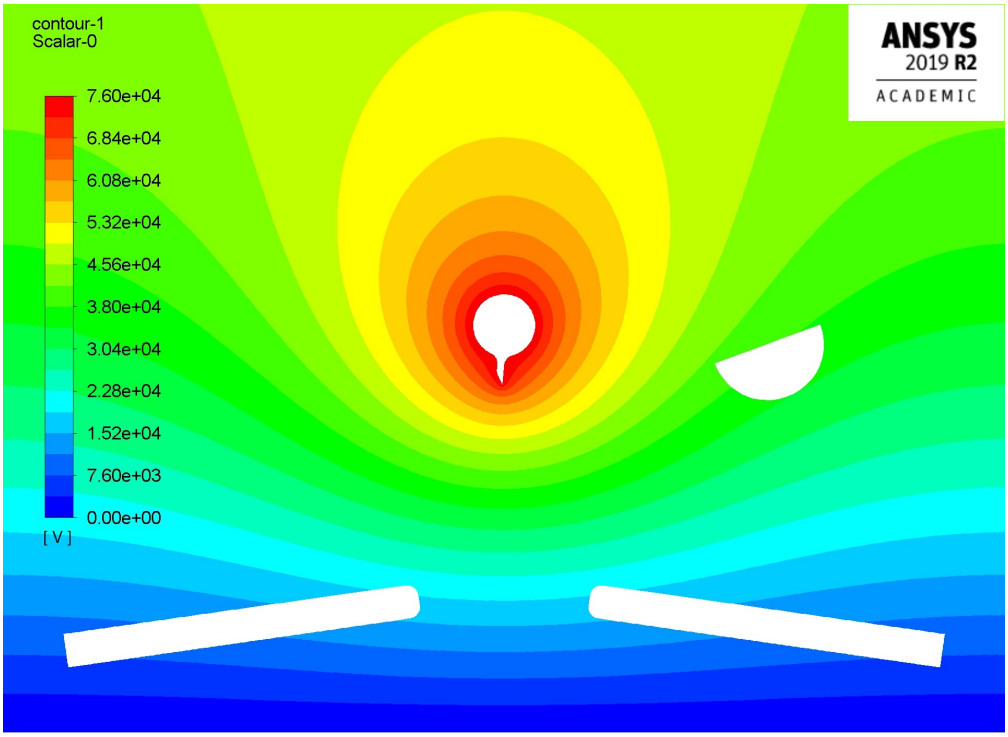

(a) $U = 76\text{kV}, \tilde{Q} = 0\text{g(sm)}^{-1}$.

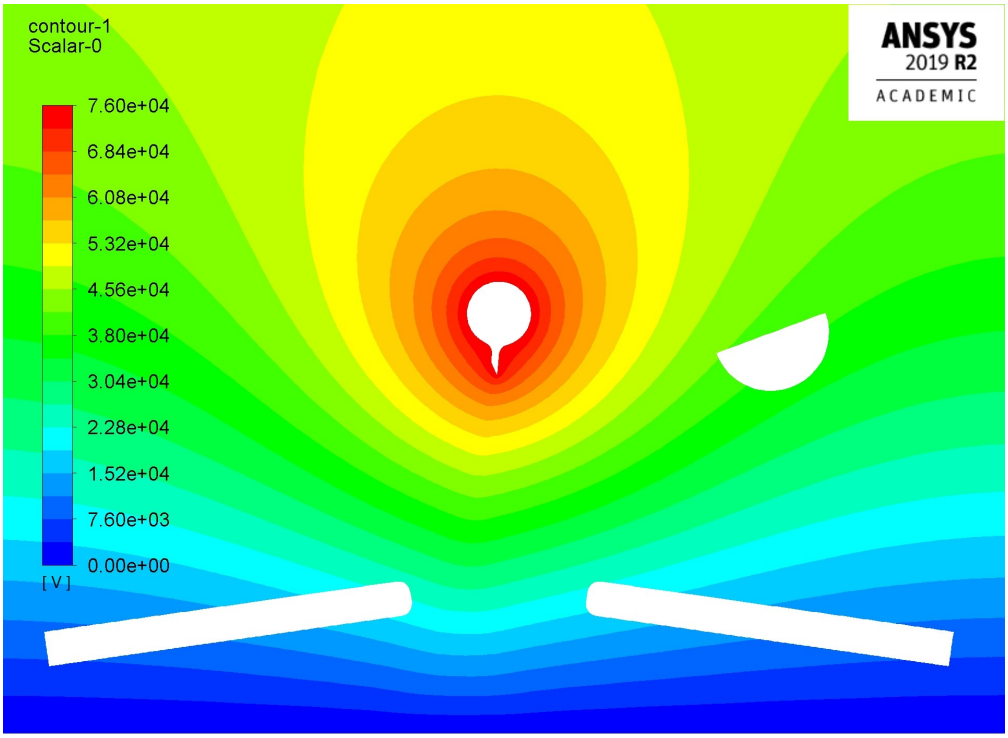

(b) $U = 76\text{kV}, \tilde{Q} = 1.5\text{g(sm)}^{-1}$.

Figure 5.6: Simulated electric potential.

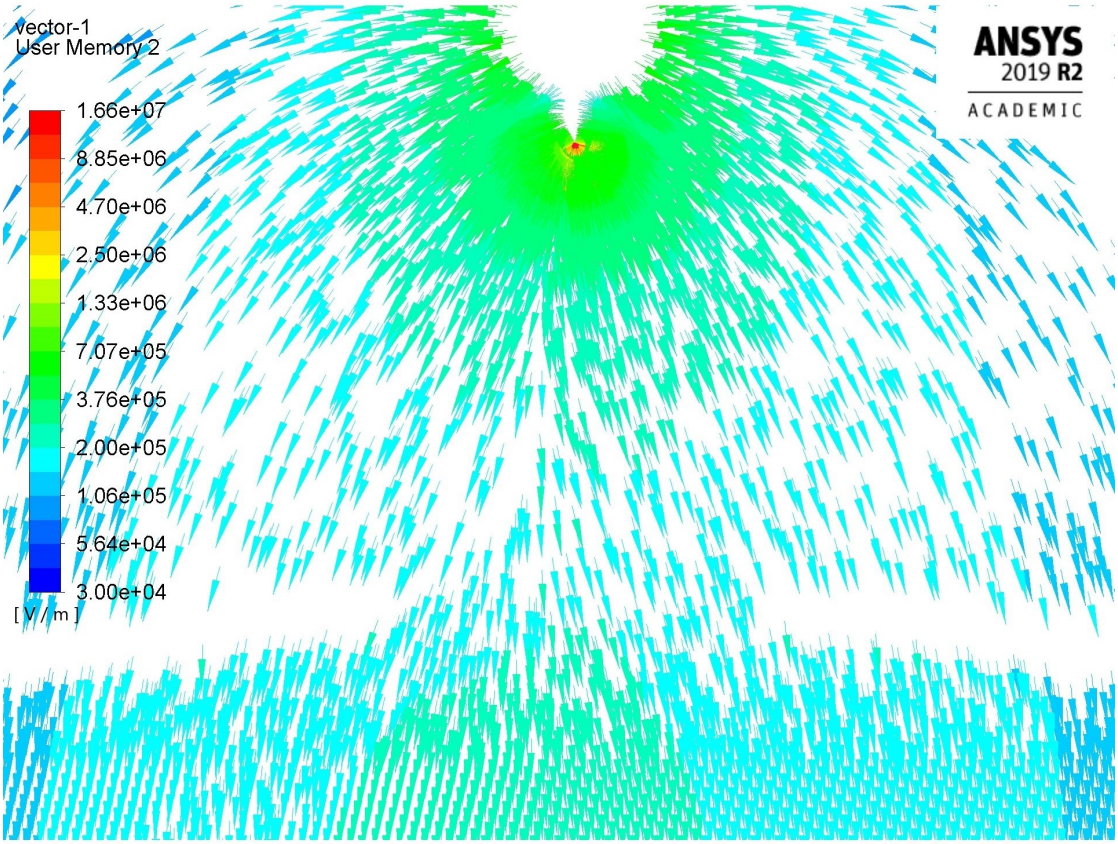

Figure 5.7: Simulated electric field for $U = 76\text{kV}, \tilde{Q} = 1.5\text{g(sm)}^{-1}$.

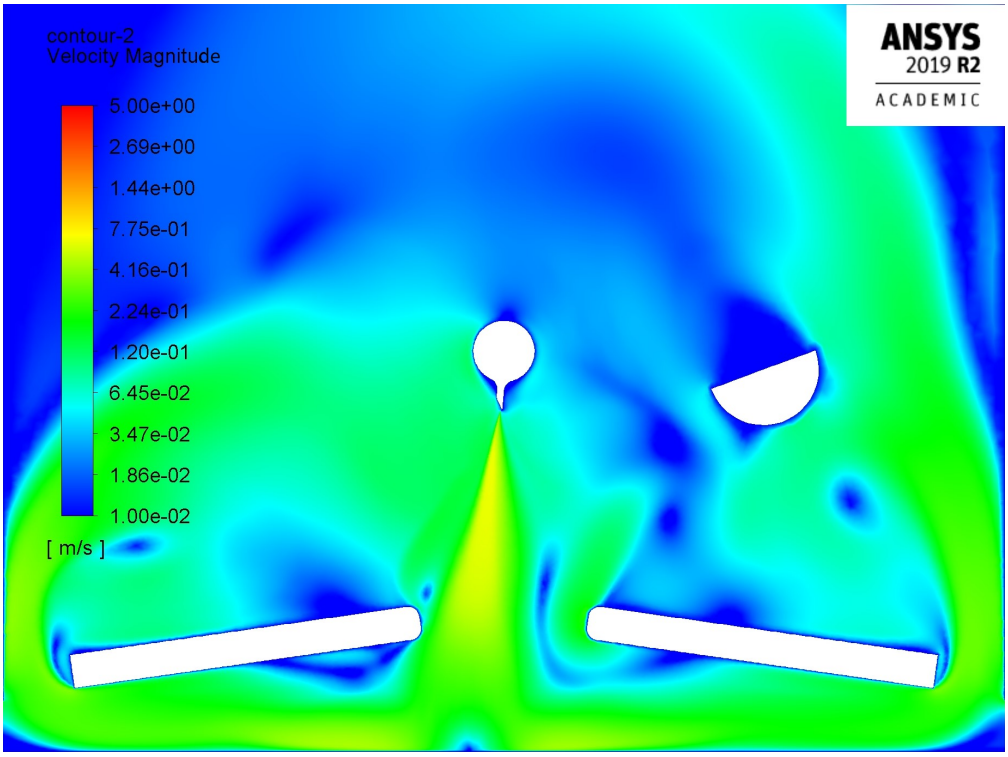

(a) $v_{\text{strip}} = 0\text{ms}^{-1}$.

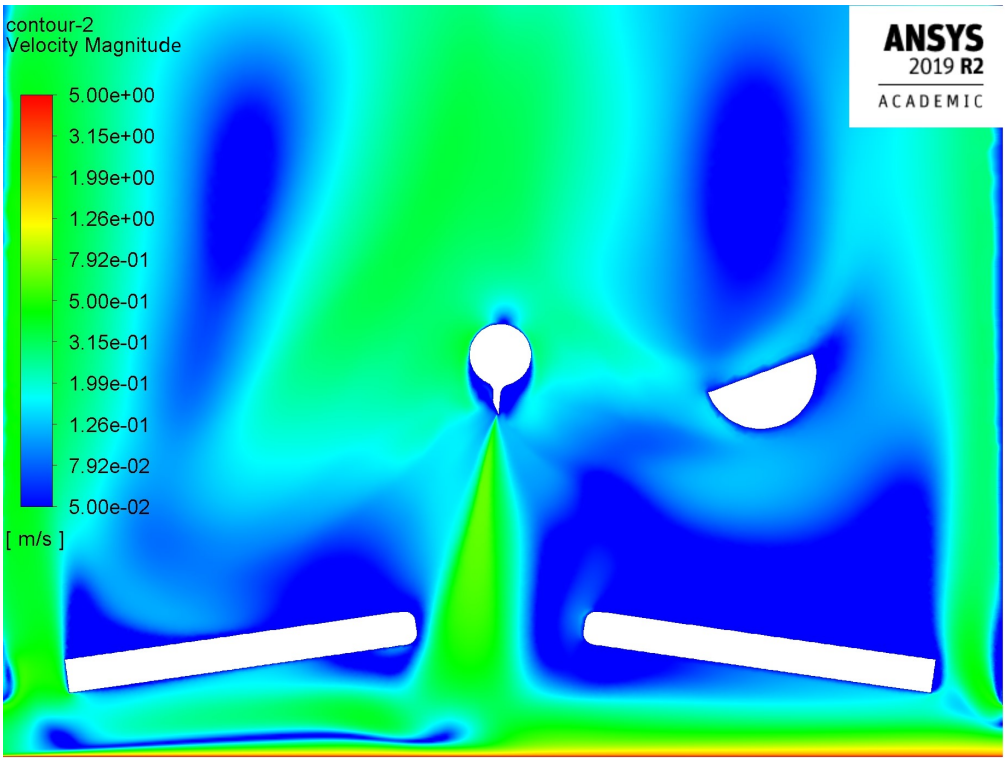

(b) $v_{\text{strip}} = 5\text{ms}^{-1}$.

Figure 5.8: Simulated magnitude of the air flow velocity for $U = 76\text{kV}, \tilde{Q} = 1.5\text{g(sm)}^{-1}$.

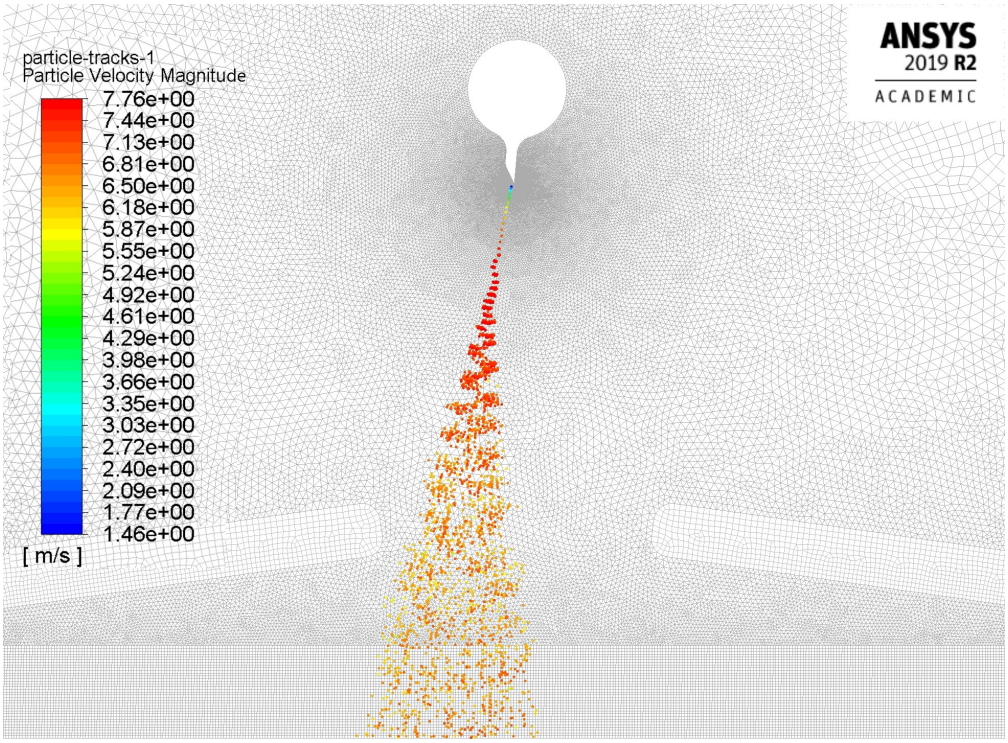

(a) Droplet velocities.

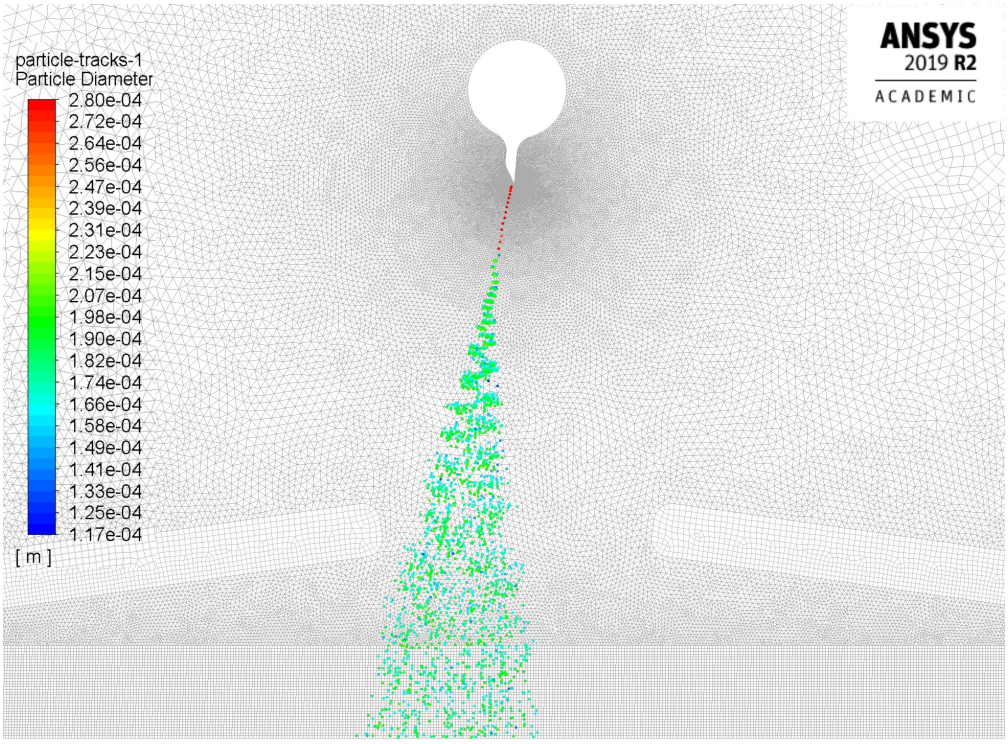

(b) Droplet diameters.

Figure 5.9: Simulated droplet trajectories for $U = 50\text{kV}, \tilde{Q} = 1.5\text{g(sm)}^{-1}, v_{strip} = 5\text{ms}^{-1}$.

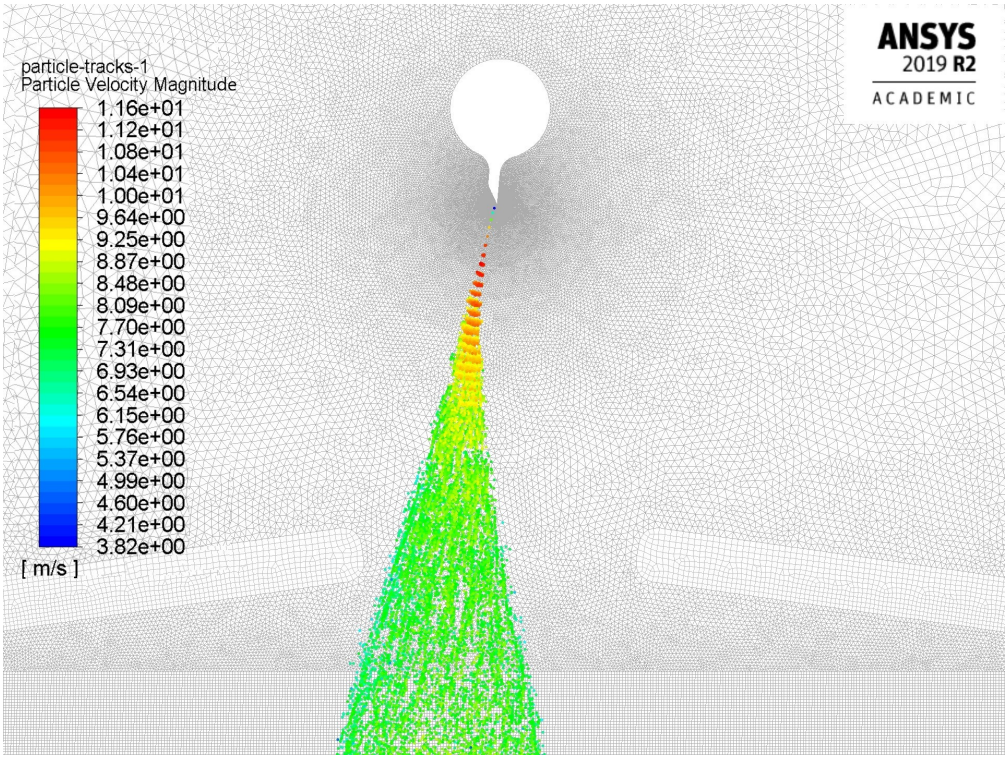

(a) Droplet velocities.

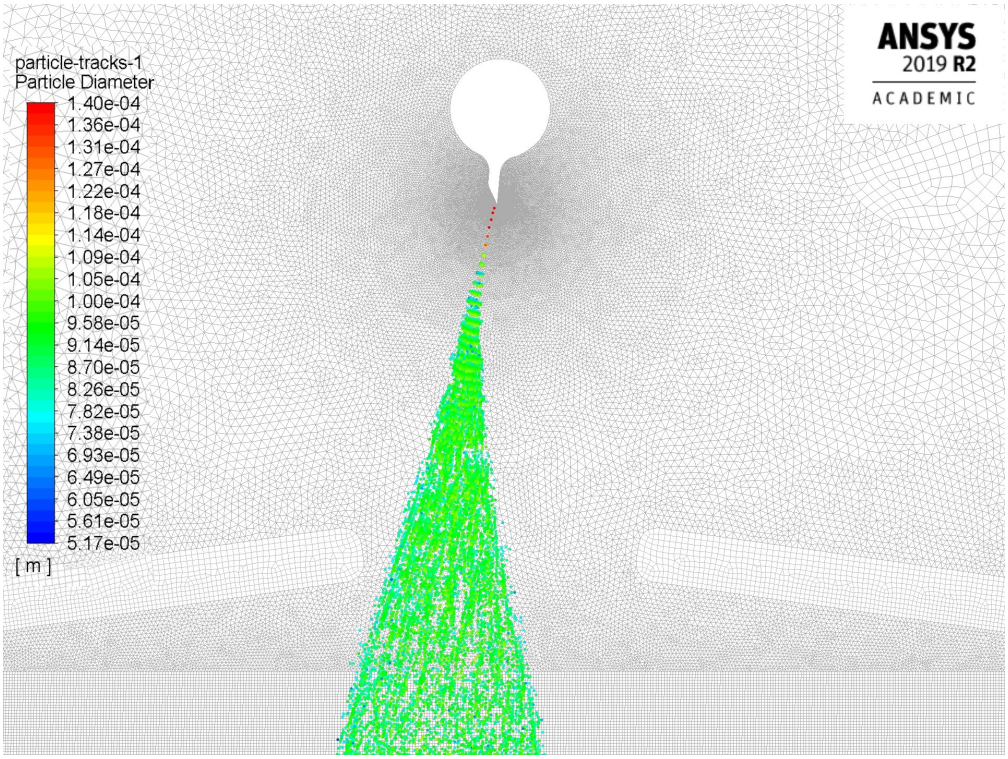

(b) Droplet diameters.

Figure 5.10: Simulated droplet trajectories for $U = 105\text{kV}, \tilde{Q} = 1.5\text{g(sm)}^{-1}, v_{strip} = 5\text{ms}^{-1}$.

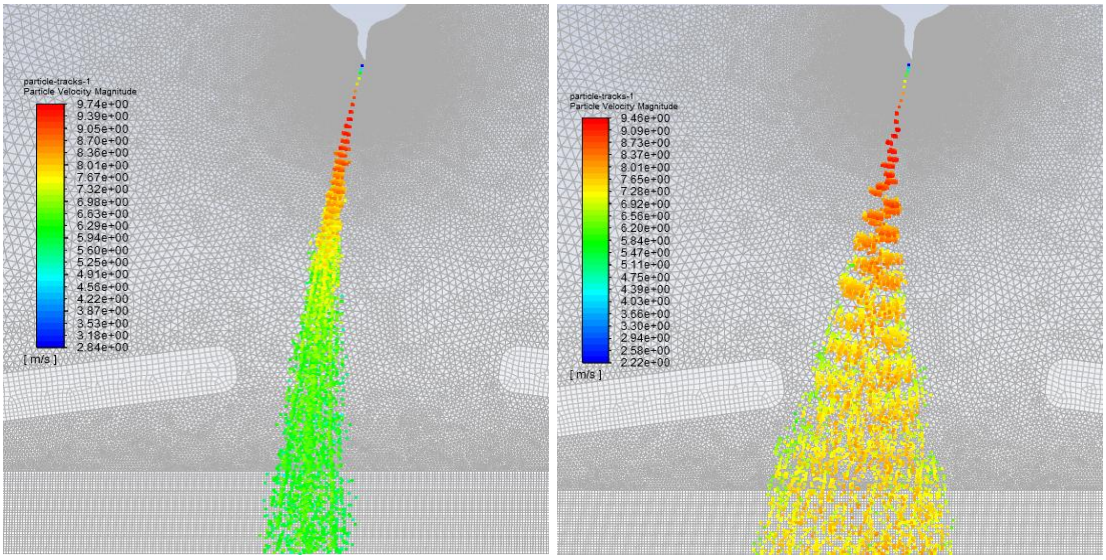

(a) $\tilde{Q} = 0.4\text{g(sm)}^{-1}$. (b) $\tilde{Q} = 1.8\text{g(sm)}^{-1}$.

Figure 5.11: Simulated droplet trajectories for $U = 75\text{kV}$ and different oil mass flow rates per meter $\tilde{Q}$.

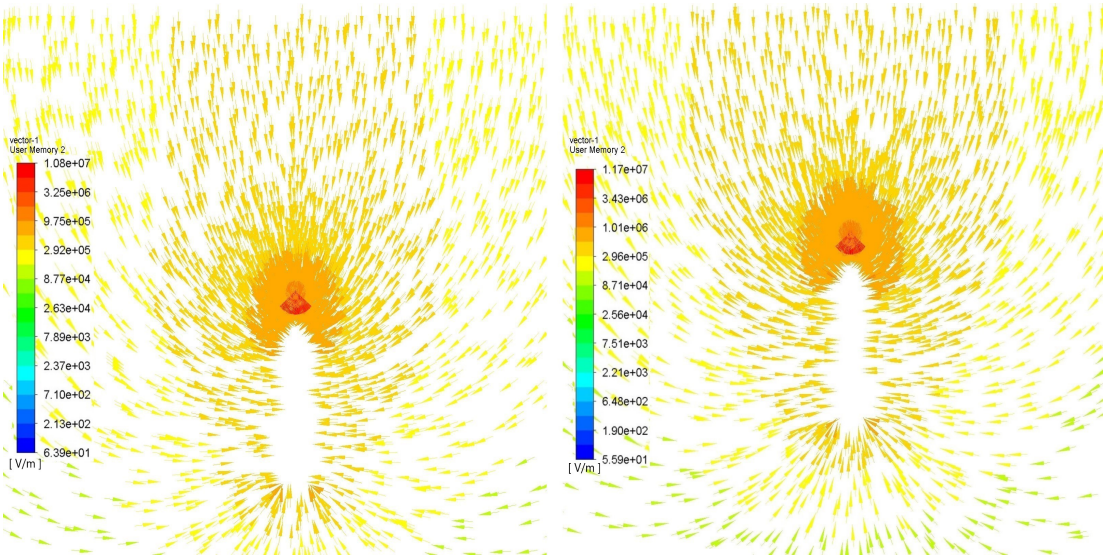

(a) 160mm distance between blade and strip. (b) 135mm distance between blade and strip.

Figure 5.12: Electric field around the lower blade.

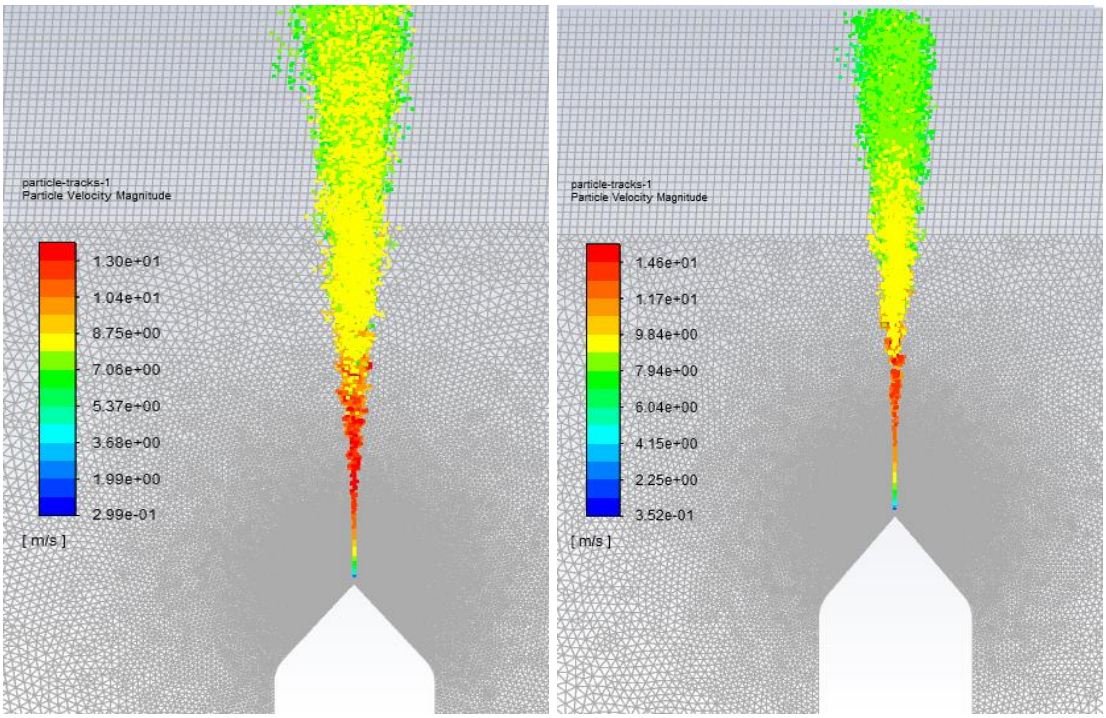

(a) 160mm distance between blade and strip. (b) 135mm distance between blade and strip.

Figure 5.13: Droplet velocities of the lower blade.

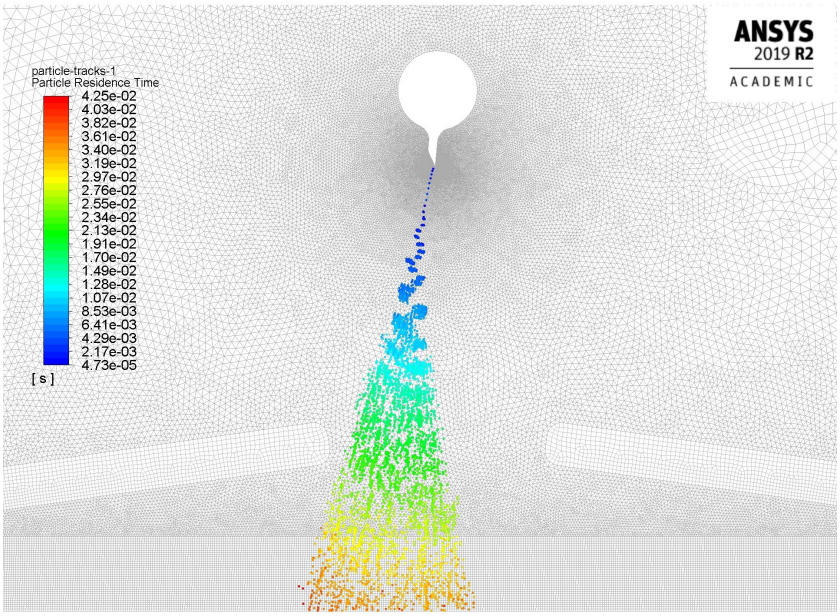

Figure 5.14: Droplet traveling time for $U = 75\text{kV}, \tilde{Q} = 1.5\text{g(sm)}^{-1}$.

Position	Drag force (N)	Gravitational force (N)	Electrostatic force (N)
		Upper blade	
A	$2.2 \cdot 10^{-6}$	$3.1 \cdot 10^{-8}$	$3.8 \cdot 10^{-5}$
B	$9.3 \cdot 10^{-7}$	$1.0 \cdot 10^{-8}$	$7.4 \cdot 10^{-7}$
C	$8.8 \cdot 10^{-7}$	$1.0 \cdot 10^{-8}$	$5.7 \cdot 10^{-7}$
		Lower blade	
A	$1.1 \cdot 10^{-6}$	$1.5 \cdot 10^{-7}$	$9.2 \cdot 10^{-5}$
B	$4.3 \cdot 10^{-7}$	$2.3 \cdot 10^{-9}$	$4.2 \cdot 10^{-7}$
C	$3.5 \cdot 10^{-7}$	$2.3 \cdot 10^{-9}$	$2.8 \cdot 10^{-7}$

Table 5.3: Comparison of forces acting on the droplets, positions according to Fig. 5.15.

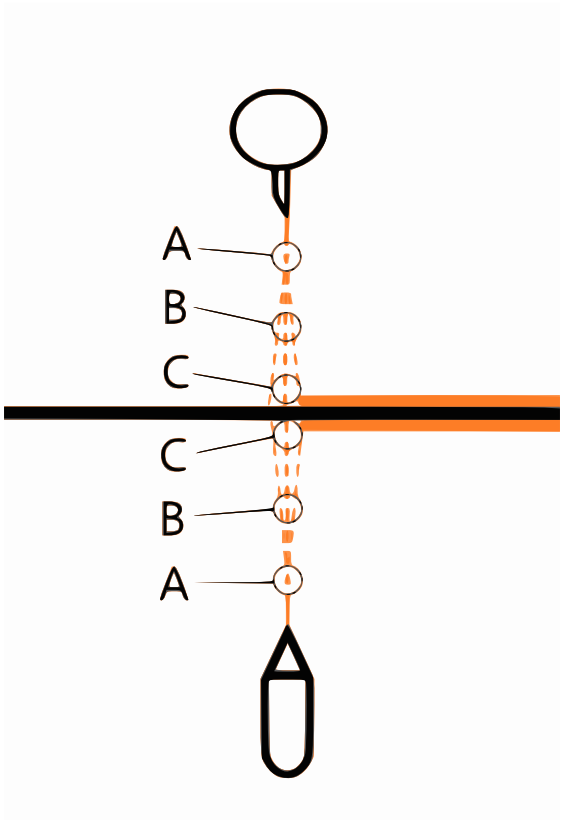

Figure 5.15: Positions where the forces are evaluated (summarized in Tab. 5.3).

6 Effect of an Inclined Oiler Blade on the Oil Distribution

This chapter deals with the problem of an inclined upper oiler blade, which means that the blade does not have the same vertical position at the operator side and at the drive side as illustrated in Fig. 6.1. A small incline may occur due to vibrations or temperature changes. An incline can lead to a non-uniform oil distribution on the blade as depicted in Fig. 6.1 and thus also on the strip, as shown in Fig. 6.4.

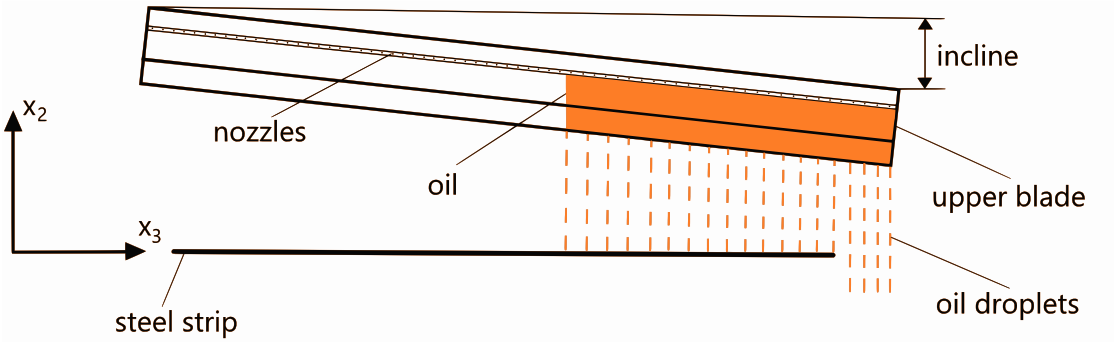

Figure 6.1: Inclined upper blade.

At the lower blade, the oil nozzles are located at the topmost position of the oil cavity as shown in Fig. 2.3. This is not the case at the upper blade, where the nozzles are located at a lateral position of the oil cavity. Consequently, air in the volume above the nozzles cannot escape as illustrated in Fig. 6.2. Essentially, the air accumulates at the elevated side of the inclined blade, whereas most of the oil flows out at the lower side. As indicated in Fig. 6.2, a rotation of the blade with respect to its lateral axis changes the air volume. It was found that a smaller remaining air volume also reduces the dependence of the oil distribution on the slope of the blade. However, the blade cannot be rotated too far because the oil spray would hit the protection plates of the oiling machine as shown in Subfigure 6.3(a). For $U = 75\text{kV}$ and $\tilde{Q} = 3.0\text{g(sm)}^{-1}$, the maximum useful rotation angle of the upper blade is 20° as shown in Subfigure 6.3(b). This rotation angle was tested for an incline of 5mm. The rotation improves the oil distribution on the strip as the comparison of region (b) and region (c) in Fig. 6.4 shows. The rotation of the blade is a simple option to improve the oil distribution on the strip.

Another option to reduce the dependence of the oil distribution on the incline would be a bleed valve installed at the topmost position of the oil chamber in the blade. A third option would be an improved design of the cross section of the blade.

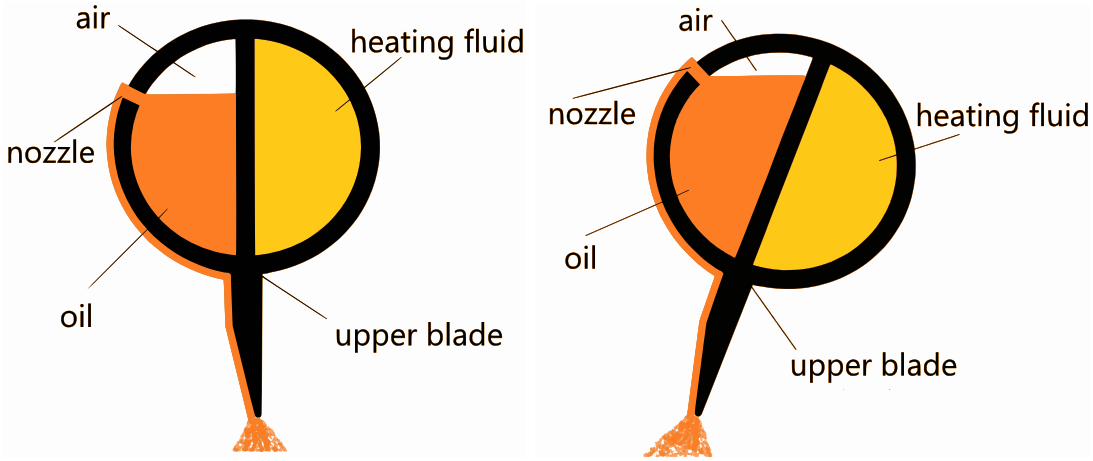

(a) Original blade position. (b) 20° rotated blade.

Figure 6.2: Air volume in upper blade.

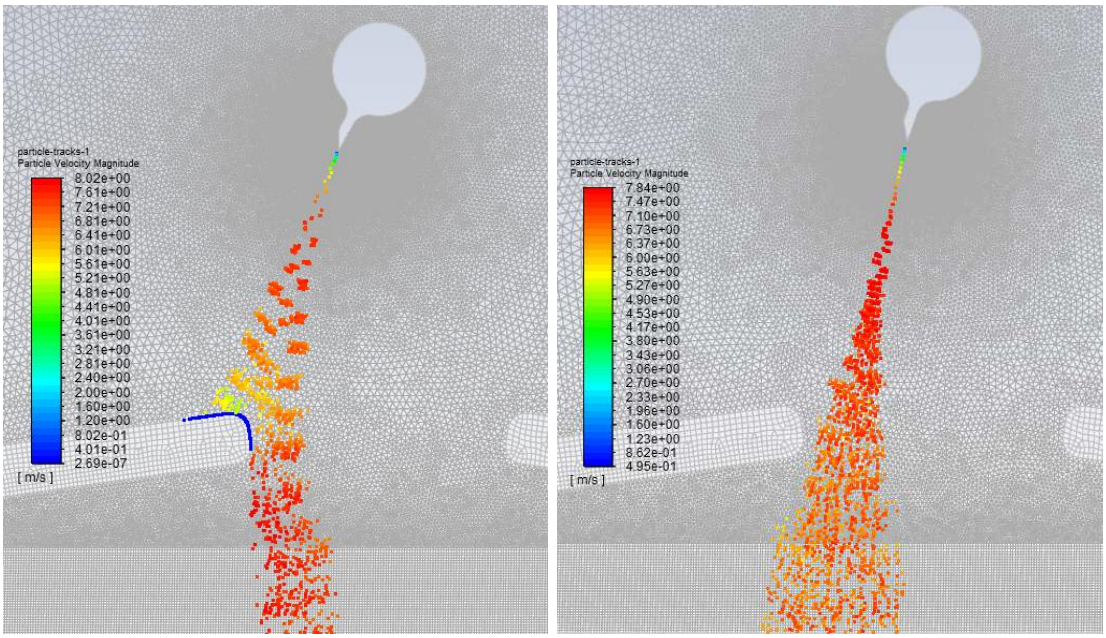

(a) 30° rotation angle. (b) 20° rotation angle.

Figure 6.3: Simulated oil droplet trajectories for a rotated blade, $U = 75\text{kV}$ and $\tilde{Q} = 3.0\text{g(sm)}^{-1}$.

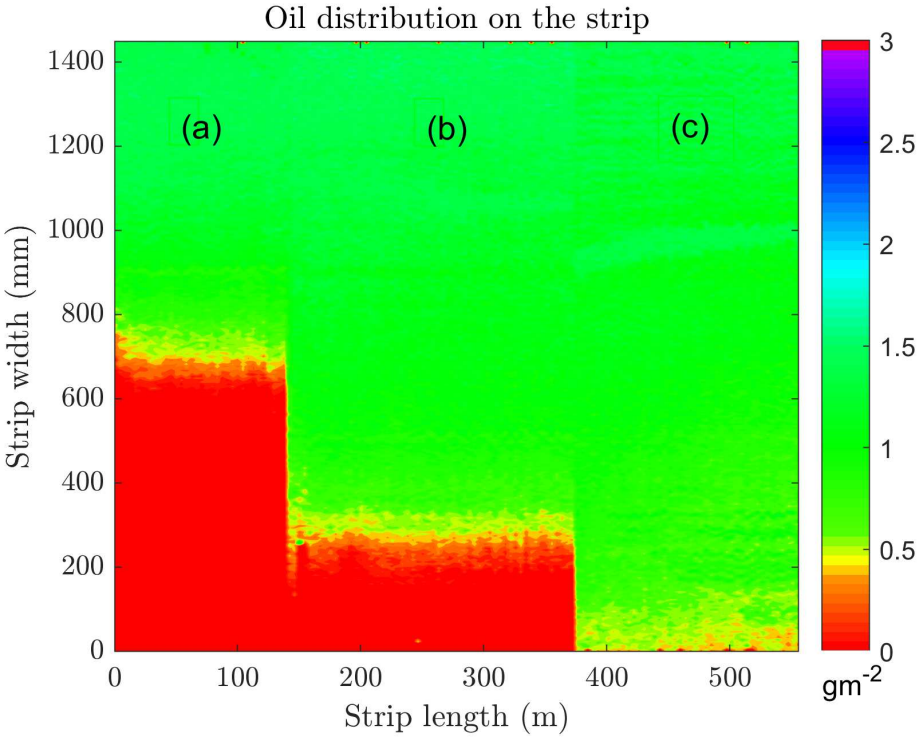

Figure 6.4: Measured oil distribution on the upper side of the strip for 25 mm incline and original blade angle (a), 5 mm incline and original blade angle (b), 5 mm incline and 20° rotated blade (c).

7 Conclusions and Future Work

The simulation results of the developed mathematical model of the electrostatic oiling machine show a good agreement with measured data and only one set of parameters is needed for the considered operational conditions. In addition, the simulated droplet diameters match the theoretical predictions of the Rayleigh limit. In contrast to other works, the presented model includes a droplet breakup model, which is necessary to achieve the desired accuracy.

It was found that the oil is not atomized in the immediate vicinity of the blade tip but oil cones are formed. Oil jets start at the tip of these cones. These jets break up into droplets after a few centimeters due to the repulsive forces between the charges. The formation of stable oil cones and oil jets requires a minimum voltage.

The droplets formed after the breakup of the oil jets are accelerated due to the high field strength. The corresponding electrostatic force is about ten times higher than the drag force in the vicinity of the blade. The droplets are accelerated until the velocity-dependent drag force exceeds the electrostatic force. The calculations show that the gravitation acting on the droplets is small compared to the other forces. The flight time of the droplets is about 40 ms from the upper blade tip to the strip. During this time span the strip moves 20 cm. Hence, a change of the oil mass flow rate at the blade tip immediately changes the amount of oil on the strip.

Moreover, the simulations show that the droplet velocities increase with increasing blade voltages. In addition, the droplets carry more charge with increasing voltage. As a consequence, the droplets break up into smaller droplets and the oil spray is widened. A lower distance between the blade and the strip also leads to an increase in the electric field strength and to an increase of the droplet velocities and to smaller droplets. The evaluation of the electric field shows that it is more than ten times higher at the blade tip compared to other positions on the blade surface or below it. This is why the oil jet formation takes place directly at the blade tip. The calculation results show that the droplet trajectories are practically unaffected by the boundary layer air flow next to the moving strip.

Table 7.1 summarizes the dependence of the output variables, i.e. droplet diameter d, the droplet velocity magnitude u, the charge q_d on the droplets, the droplet travel time t_{travel} from the blade to the strip, the spray width, and the air velocity magnitude v on the input variables, i.e. the voltage U, the oil mass flow rate Q, and the strip velocity v_{strip}.

It was found that an inclined upper blade leads to a non-uniform oil distribution on the strip. The oil is already non-uniformly distributed on the oiler blade because air remains in the blade above the nozzles and accumulates at the elevated side of the blade. A rotation of the blade with respect to its lateral axis reduces the dependence of the

Input		Output					
		d	u	q_d	t_{travel}	Spray width	v
U	$\uparrow$	$\downarrow$	$\uparrow$	$\uparrow$	$\downarrow$	$\uparrow$	$\uparrow$
Q	$\uparrow$	$\simeq$	$\simeq$	$\downarrow$	$\simeq$	$\uparrow$	$\uparrow$
v_{strip}	$\uparrow$	$\simeq$	$\simeq$	$\simeq$	$\simeq$	$\simeq$	$\uparrow$

Table 7.1: Dependence of the output variables on the input variables.

oil distribution on the incline of the blade because the remaining air volume is reduced. Another suggestion to improve the oil distribution is a bleed valve at the topmost of the upper oiler blade.

The presented model was validated for one oil type. The model should be validated for other oil types in future works. Furthermore, the influence of the temperature was not considered here. According to [9], there is an optimum range of the oil viscosity and surface tension for a good spraying behavior. Since these two quantities depend on temperature, further optimization possibilities could be identified in a future work.

The mentioned oil cones are described in the literature in the case of single cones where the oil is delivered via a capillary tube. The formation of many cones located side by side along an oiler blade could also be a subject of future research.

The steel strips are coiled at the end of the process, where a redistribution of the oil takes place. Maybe a non-uniform oiling of the steel strip could compensate this redistribution.

The presented model does not include the oil jets and the charging process of the oil at the blade tip. Hence, the initial droplet diameter d_{init} and the current I are additional input variables of the model and have to be measured. An extension to calculate the oil jet diameters (initial droplet diameters) and the current as a function of the voltage, the oil mass flow rate, the blade geometry, and so on, to get a stand-alone model, could also be subject of future works.

A Appendix

A.1 Oil Properties

density ρ_d (kgm^{-3})	viscosity ν_d (mm^{2}s^{-1})	surface tension γ (Nm^{-1})
892 (20°C)	26 (40°C)	0.03 [9], [43]

Table A.1: Oil properties.

A.2 Comparison of Two Different Types of Droplet Injection.

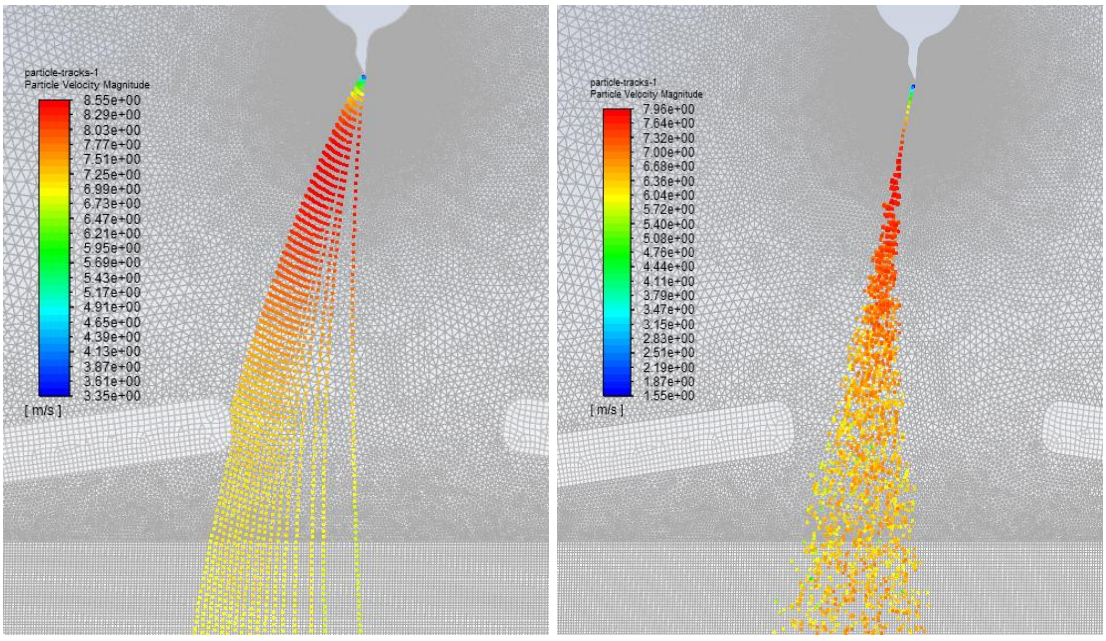

(a) Injection of droplets side by side without droplet breakup.

(b) Droplet injection at one point with droplet breakup.

Figure A.1: Comparison of two different types of droplet injection.

Bibliography

[1] E. L. Ergene, "Investigation of the electrostatic atomization method for remote injection and high pressure," PhD thesis, Middle East Technical University, Beirut, Libanon, 2006.

[2] S. A. Colbert, "Numerical simulations of droplet trajectories from an electrostatic rotary-bell atomizer," PhD thesis, Drexel University, Philadelphia, USA, 2006.

[3] K. R. Ellwood and J. Braslaw, "A finite-element model for an electrostatic bell sprayer," *Journal of Electrostatics*, vol. 45, pp. 1–23, 1998.

[4] Q. Ye, T. Steigleder, A. Scheibe, and J. Domnick, "Numerical simulation of the electrostatic powder coating process with a corona spraygun," *Journal of Electrostatics*, vol. 54, pp. 189–205, 2002.

[5] J. D. Q. Ye, "On the simulation of space charge in electrostatic powder coating with a corona spray gun," *Powder Technology*, vol. 135, pp. 250–260, 2003.

[6] N. Toljic, K. Adamiak, G. Castle, H.-H. Kuo, and H.-T. Fan, "A full 3d numerical model of the industrial electrostatic coating process for moving targets," *Journal of Electrostatics*, vol. 71, pp. 299–304, 2013.

[7] S. Zhao, K. Adamiak, and G. S. P. Castle, "The implementation of poisson field analysis within fluent to model electrostatic spraying," *Proceedings of the Canadian Conference on Electrical and Computer Engineering*, pp. 1456–1459, May 2007.

[8] Ravarini. (2019). Basic description of an electrostatic oiler, [Online]. Available: `http://www.ravarinicastoldi.it/elettrospray/elettro_ing/spec.htm` (visited on 11/29/2019).

[9] S. Foster. (2012). Electrostatic spraying with two blades on the top (temper mill oiler), [Online]. Available: `https://www.gfg-peabody.com/wp-content/uploads/2015/06/Electrostatics_TemperMill.pdf` (visited on 11/29/2019).

[10] J. D. Jackson, *Classical Electrodynamics*, 3rd ed. New York: Wiley, 1998.

[11] D. J. Acheson, *Elementary Fluid Dynamics*. Oxford University Press, 1990.

[12] O. Reynolds, "On the dynamical theory of incompressible viscous fluids and the determination of the criterion," *Philosophical Transactions of the Royal Society of London A*, vol. 186, pp. 123–164, 1895.

[13] J. O. Hinze, *Turbulence*. McGraw-Hill Publishing Co., 1975.

[14] J. J. Bertin, J. Periaux, and J. Ballmann, *Advances in Hypersonics: Modeling hypersonic flows*. Birkhäuser, 1992.

[15] B. E. Launder and D. B. Spalding, *Lectures in Mathematical Models of Turbulence*. Academic Press, 1972.

[16] H. Versteeg and W. Malalasekera, *An Introduction to Computational Fluid Dynamics: The Finite Volume Method*. Pearson Education, 2007.

[17] S. Braun, *Strömungslehre für TPh*, TU-MV Media Verlag GmbH, 2017.

[18] A. D. Gosman and E. Ioannides, "Aspects of computer simulation of liquid-fuelled combustors," *Energy Journal*, vol. 7, pp. 482–490, 1983.

[19] A. Haider and O. Levenspiel, "Drag coefficient and terminal velocity of spherical and nonspherical particles," *Powder Technology*, vol. 58, pp. 63–70, 1989.

[20] ANSYS. (2019). Ansys fluent theory guide, [Online]. Available: `https://ansyshelp.ansys.com/account/secured?returnurl=/Views/Secured/corp/v194/flu_th/flu_th.html` (visited on 12/08/2019).

[21] J. W. S. Rayleigh, "On the equilibrium of liquid conducting masses charged with electricity," *Philosophical Magazine*, vol. 5, no. 14, pp. 184–186, 1882.

[22] A. Gomez and K. Tang, "Charge and fission of droplets in electrostatic sprays," *Physics of Fluids*, vol. 6, pp. 404–414, 1994.

[23] L. De Juan and J. De La Mora Fernandez, "Charge and size descriptions of electrospray drops," *Journal of Colloid and Interface Science*, vol. 186, pp. 280–293, 1997.

[24] J. Shrimpton, "Dielectric charged drop break-up at sub-rayleigh limit conditions," *IEEE Transactions on Dielectrics and Electrical Insulation*, vol. 12, no. 3, pp. 573–578, 2005.

[25] G. I. Taylor, *The shape and acceleration of a drop in a high speed air stream, technical report*, in G.K. Batchelor, *Scientific Papers of G. I. Taylor*, Cambridge University Press, 1963.

[26] R. D. Reitz, "Mechanisms of atomization processes in high-pressure vaporizing sprays," *Atomization and Spray Technology*, vol. 3, pp. 309–337, 1987.

[27] J. C. Beale and R. D. Reitz, "Modeling spray atomization with the kelvin-helmholtz / rayleigh-taylor hybrid model," *Atomization and Sprays*, vol. 9, pp. 623–650, 1999.

[28] S. V. Apte, M. Gorokhovski, and P. Moin, "Les of atomizing spray with stochastic modeling of secondary breakup," *International Journal of Multiphase Flow*, vol. 29, pp. 1503–1522, 2003.

[29] P. Day, A. Manz, and Y. Zhang, *Microdroplet Technology: Principles and Emerging Applications in Biology and Chemistry*. Springer, 2012.

[30] ANSYS. (2010). Ansys fluent user's guide, [Online]. Available: `http://www.fluid.tuwien.ac.at/322057?action=AttachFile&do=get&target=flu_ug.pdf` (visited on 11/16/2019).

[31] Pico Technology. (2019). Measuring the shutter speed of a camera, [Online]. Available: `https://www.picotech.com/library/experiment/camera-shutter-speed` (visited on 10/28/2019).

[32] A. Bailey, "Electrostatic spraying of liquids," *Physics Bulletin*, vol. 35, pp. 146–148, 1984.

[33] K. S. Robinson and R. J. Turnbull, "Electrostatic spraying of liquid insulators," *IEEE Transactions on Industry*, vol. IA-16, no. 2, pp. 308–317, 1980.

[34] A. Jaworek and A. Krupa, "Classification of the modes of ehd spraying," *Journal of Aerosol Science*, vol. 30, no. 7, pp. 873–893, 1999.

[35] A. M. Ganan-Calvo, "Cone-jet analytical extension of taylor's electrostatic solution and the asymptotic universal scaling laws in electrospraying," *Physical Review Letters*, vol. 79, no. 2, pp. 217–220, 1997.

[36] D. Gao, D. Yao, S. K. Leist, Y. Fei, and J. Zhou, "Mechanisms and modeling of electrohydrodynamic phenomena," *International Journal of Bioprinting*, vol. 5, no. 1, 2019.

[37] S. Maktabi and P. A. Chiarot, "Electrohydrodynamic printing of organic polymeric resistors on flat and uneven surfaces," *Journal of Applied Physics*, vol. 120, 2016.

[38] O. Lastow and W. Balachandran, "Numerical simulation of electrohydrodynamic atomization," *Journal of Electrostatics*, vol. 64, pp. 850–859, 2006.

[39] G. I. Taylor, "Disintegration of water drops in an electric field," *The Royal Society Publishing*, vol. 280, no. 1382, pp. 383–397, 1964.

[40] S. Martin, A. Perea, P. L. Garcia-Ybarra, and JoseL.Castillo, "Effect of the collector voltage on the stability of the cone-jet mode in electrohydrodynamic spraying," *Journal of Aerosol Science*, vol. 46, pp. 53–63, 2012.

[41] MathWorks. (2019). Optimization toolbox: Fminsearch, [Online]. Available: `https://www.mathworks.com/help/matlab/ref/fminsearch.html` (visited on 10/20/2019).

[42] J. C. Lagarias, J. A. Reeds, M. H. Wright, and P. E. Wright., "Convergence properties of the nelder-mead simplex method in low dimensions," *SIAM Journal of Optimization*, vol. 9, no. 1, pp. 112–147, 1998.

[43] Z.-H. Wang, F.-P. Wang, J.-R. Fan, Q.-J. Gao, and J.-Q. Wang, "The spraying field characteristics and distribution of deposition of droplets of electrostatic oiler," *Journal of Engineering and Technology Research*, vol. 8, pp. 31–64, 2016.

Eidesstattliche Erklärung

Hiermit erkläre ich, dass die vorliegende Arbeit gemäß dem Code of Conduct – Regeln zur Sicherung guter wissenschaftlicher Praxis (in der aktuellen Fassung des jeweiligen Mitteilungsblattes der TU Wien), insbesondere ohne unzulässige Hilfe Dritter und ohne Benutzung anderer als der angegebenen Hilfsmittel, angefertigt wurde. Die aus anderen Quellen direkt oder indirekt übernommenen Daten und Konzepte sind unter Angabe der Quelle gekennzeichnet. Die Arbeit wurde bisher weder im In– noch im Ausland in gleicher oder in ähnlicher Form in anderen Prüfungsverfahren vorgelegt.

Vienna, December 2019

Julian Landauer